

THE DETECTION OF C₆₀ IN THE WELL-CHARACTERIZED PLANETARY NEBULA M1-11MASAAKI OTSUKA^{1,2}, F. KEMPER¹, S. HYUNG³, B. A. SARGENT^{2,4}, M. MEIXNER², A. TAJITSU⁵, K. YANAGISAWA⁶¹Institute of Astronomy and Astrophysics, Academia Sinica P.O. Box 23-141, Taipei 10617, Taiwan, R.O.C.; otsuka@asiaa.sinica.edu.tw²Space Telescope Science Institute, 3700 San Martin Drive, Baltimore, MD 21218, U.S.A.³School of Science Education (Astronomy), Chungbuk National University, Cheongju, Chungbuk 361-763, Korea⁴Center for Imaging Science and Laboratory for Multiwavelength Astrophysics, Rochester Institute of Technology, 54 Lomb Memorial Drive, Rochester, NY 14623, USA⁵Subaru Telescope, NAOJ, 650 North A'ohoku Place, Hilo, Hawaii 96720, U.S.A. and⁶Okayama Astrophysical Observatory (OAO), NAOJ, Kamogata, Okayama 719-0232, Japan

(Received; Revised; Accepted)

ABSTRACT

We performed multiwavelength observations of the young planetary nebula (PN) M1-11 and obtained its elemental abundances, dust mass, and the evolutionary status of the central star. The *AKARI*/IRC, VLT/VISIR, and *Spitzer*/IRS spectra show features due to carbon-rich dust, such as the 3.3, 8.6, and 11.3 μm features due to polycyclic aromatic hydrocarbons (PAHs), a smooth continuum attributable to amorphous carbon, and the broad 11.5 and 30 μm features often ascribed to SiC and MgS, respectively. We also report the presence of an unidentified broad feature at 16–22 μm , similar to the feature found in Magellanic Cloud PNe with either C-rich or O-rich gas-phase compositions. We identify for the first time in M1-11 spectral lines at 8.5 (blended with PAH), 17.3, and 18.9 μm that we attribute to the C₆₀ fullerene. This identification is strengthened by the fact that other Galactic PNe in which fullerenes are detected, have similar central stars, similar gas-phase abundances, and a similar dust composition to M1-11. The weak radiation field due to the relatively cool central stars in these PNe may provide favorable conditions for fullerenes to survive in the circumstellar medium. Using the photo-ionization code CLOUDY, combined with a modified blackbody, we have fitted the ~ 0.1 –90 μm spectral energy distribution and determined the dust mass in the nebula to be $\sim 3.5 \times 10^{-4} M_{\odot}$. Our chemical abundance analysis and SED model suggest that M1-11 is perhaps a C-rich PN with C/O ratio in the gas-phase of +0.19 dex, and that it evolved from a 1–1.5 M_{\odot} star.

Subject headings: ISM: planetary nebulae: individual (M1-11), ISM: abundances

1. INTRODUCTION

The most stable fullerene is C₆₀ (Draine 2011). Fullerenes together with other carbon dust such as graphite are expected to be important components of the interstellar medium (ISM), because they contribute to interstellar extinction. For example, Dopita et al. (1997) argued the possibility that the deep 2200 Å absorption feature in the low-excitation planetary nebula (PN) SMP LMC8 might be by a surface charge slop resonance on C₆₀. The graphite grains have a spectral peak around this wavelength due to $\pi \rightarrow \pi^*$ electron excitations. Fullerene and polycyclic aromatic hydrocarbons (PAHs) resemble graphite; therefore such grains have strong electronic transitions around 2200 Å (Draine 2011). The investigation of circumstellar carbon grains such as C₆₀ would be important to understand ISM evolution more deeply.

Recent *Spitzer*/IRS studies show that fullerenes C₆₀ are detected in several young PNe, a proto-PN, and two post asymptotic giant branch stars (post AGB) in the Milky Way (Cami et al. 2010; García-Hernández et al. 2010; Zhang & Kwok 2011; Gielen et al. 2011) and also in a handful young PNe in the Magellanic Clouds (García-Hernández et al. 2011a; Bernard-Salas et al. 2012). The detection cases are increasing, however the excitation and formation mechanism is still unclear (e.g., Cami et al. 2011; García-Hernández 2012). The detections generally suggest that fullerenes can survive or be observed in a C-rich environment with a weak radiation field.

M1-11 (PN G232.8–04.7) is a good sample in C₆₀ formation in a circumstellar environment, because most of the C₆₀ PNe have cool central stars ($\sim 30,000$ K) and C-rich nebulae, and they are very young (~ 1000 yr). Indeed, M1-11 has the

cool central star (29 300 K, Phillips 2003), and the nebula is relatively compact, with a size of $\lesssim 6''$ in diameter in H α emission, and it appears to be a very young object (~ 1000 yr after leaving the AGB phase, this paper). Henry et al. (2010) measured the C abundance in M1-11 using recombination lines (RLs) and the O abundance with collisionally excited lines (CELs, number density ratio of C/O = 79.4). To date, only upper limits to the intensities of the CELs C III] 1906 and 1909 Å are obtained (Kingsburgh & Barlow 1994), and thus the gas phase C/O ratio of M1-11 derived from the same type of emission line is still unknown. However, M1-11 is also known to be a dust-rich PN, showing predominantly C-rich dust. Silicon carbide (SiC) and amorphous silicate features are seen in the *IRAS*/LRS data (Zhang & Kwok 1990). A significant near-infrared excess suggests the presence of hot dust (Phillips & Ramos-Larios 2005; Zhang & Kwok 1990), although there is also a contribution from the 3.3 μm emission feature due to PAHs in the near infrared (Allen et al. 1982). Longer wavelength emission features at 6.2, 6.9, 7.7, and 8.6 μm due to PAHs are reported by Cohen et al. (1986). A very weak and tentative feature is seen around 6.9–7.0 μm (see Cohen et al. 1986). Indeed, there are other C₆₀ transitions at 7.0 and 8.5 μm but Cohen et al. (1986) show some evidence (although the quality of their data is not satisfactory) for a possible detection also in M1-11. Therefore, M1-11 is perhaps a C-rich PN.

To confirm whether C₆₀ in M1-11 is real and also obtain insights about C₆₀ formation, we need to investigate the physical and chemical properties of the dust and ionized nebula and the nature of the central star, then we need to compare

the derived quantities with those in C₆₀ PNe. To characterize M1-11, we obtained continuous data from the UV to the far-infrared using several instruments, and we comprehensively investigated this PN.

In this paper, we discuss C₆₀ in M1-11 based on the information of the dust and gas compositions and the evolutionary status of the central star. In section 2, we describe the UV-to mid-infrared (mid-IR) spectroscopic data from the International Ultraviolet Explorer (*IUE*), Subaru/HDS, OAO/ISLE, *AKARI*/IRC, VLT/VISIR, and *Spitzer*/IRS, as well as narrow-band imaging obtained with WFPC2 on the Hubble Space Telescope (*HST*). The description in Section 2.6 includes a list of dust features seen in M1-11, specifically, we report the discovery of weak features at 8.5, 17.3 and 18.9 μm lines, which are attributed to the C₆₀ fullerenes. The derivation of the ionic and elemental abundances in the ionized nebula is given in Section 3. In Section 4, we discuss the observed C and O gas abundances and compare them with the predictions from nucleosynthesis models for AGB stars. Using the photoionization code CLOUDY (Ferland et al. 1998), we fitted the spectral energy distribution (SED) and determined the dust mass and the evolutionary status of the central star. Section 4 also includes a discussion on the formation of C₆₀, and a comparison of the physical properties of M1-11 to those of other Galactic PNe that exhibit fullerene features. A summary and future prospects are given in Section 5.

2. OBSERVATIONS AND DATA REDUCTION

2.1. Subaru/HDS observations

We obtained optical spectra of M1-11 using the High-Dispersion Spectrograph (HDS; Noguchi et al. 2002) attached to one of the two Nasmyth foci of the 8.2-m Subaru telescope, on October 6, 2008 (program ID: S08B-110, PI: M.Otsuka) and October 18, 2005 (PI: A.Tajitsu). The spectra were taken in two wavelength ranges: 3600–5400 \AA (the blue spectra, taken in 2008) and 4600–7500 \AA (the red spectra, taken in 2005).

When we obtained the blue spectra, an atmospheric dispersion corrector (ADC) was used to minimize the differential atmospheric dispersion over the broad wavelength region. We used a slit width of 1.''2 (0.6 mm) and a 2 \times 2 on-chip binning. We set the slit length to be 8.'' (4.0 mm), which fitted the nebula well and allowed us to directly subtract sky background from the object frames. The slit position angle (P.A.) was $\sim 225^\circ$. The CCD sampling pitch along the slit length projected on the sky was $\sim 0.''276$ per binned pixel. The resolving power reached around $R > 33\,000$, which is derived from the mean of the full width at half maximum (FWHM) of narrow Th-Ar and night sky lines. The total exposure time was 600 sec (=300 sec \times 2 frames). For the flux calibration, blaze function correction, and airmass correction, we observed G192B2B as a standard star.

For the red spectra, we used the red image de-rotator and set it to P.A.= 90° . We set the slit width to 0.''6 and the slit length to 7.'' and selected a 1 (wavelength dispersion) \times 2 (spatial direction) on-chip binning. The resulting spectral resolution R is $> 65\,000$. We used an exposure time of 300 sec and observed G192B2B as a standard star.

For both sets of observations, we took several bias, instrumental flat lamp, and Th-Ar comparison lamp frames. We are interested in detecting weak C, N, and O recombination lines. The peak intensities of these lines are typically ~ 10 –20% higher than the local continuum, and therefore a high

signal-to-noise ratio (S/N) of the continuum is necessary. The resulting S/N after subtraction of the sky background was found to range from ~ 5 at ~ 3700 \AA to ~ 30 at ~ 5200 \AA in the blue spectrum, and from ~ 5 at ~ 4800 \AA to 15 at ~ 6700 \AA in the red one.

Data reduction of the Subaru/HDS spectra and analysis of the emission lines was done with the long-slit reduction package `nao.twodspec` available in IRAF⁷, and was performed in the same manner as described by Otsuka et al. (2010). When measuring the fluxes of the emission-lines, we assumed that the line profiles were Gaussian and we applied a multiple Gaussian fitting technique.

The line fluxes were de-reddened using

$$\log_{10} \left[\frac{I(\lambda)}{I(\text{H}\beta)} \right] = \log_{10} \left[\frac{F(\lambda)}{F(\text{H}\beta)} \right] + c(\text{H}\beta)f(\lambda), \quad (1)$$

where $I(\lambda)$ and $F(\lambda)$ are the de-reddened and the observed fluxes at λ , respectively, and $f(\lambda)$ is the interstellar extinction parameter at λ , from the reddening law of Cardelli et al. (1989) with $R_V = 3.1$. The interstellar reddening correction was performed using the reddening coefficient $c(\text{H}\beta)$, at H β . We compared the observed Balmer line ratios of H γ (blue spectrum) or H α (red spectrum) with H β to the theoretical ratio computed by Storey & Hummer (1995) assuming the electron temperature $T_e = 10^4$ K and the electron density $n_e = 10^4$ cm⁻³ assuming that the nebula is optically thick in Ly- α (Case B of Baker & Menzel 1938). We derived $c(\text{H}\beta) = 1.677 \pm 0.008$ for the blue and 1.218 ± 0.017 for the red spectra.

The flux scaling was performed using all emission lines detected in the overlap region between the blue and the red spectra. The de-reddened relative intensities $I(\lambda)$ detected in both spectra are consistent within 10% of each other. The combined de-reddened spectrum is presented in Fig. 1, and the detected lines are listed in the Appendix (Table 16). We have detected over 160 emission lines, thus exceeding the number of detections by Henry et al. (2010), who report more than 70 lines in the 3700–9600 \AA spectra. Our measurements of the line intensities $I(\lambda)$ are in agreement with the results from Henry et al. (2010) within a $\sim 14\%$ error.

Specifically, we detected C II, N II, and O II RLs, and highly excited lines due to He II, C III, and N III. These high excitation lines show a relatively broad FWHM (~ 0.8 – 1.6 \AA) compared to typical nebular lines (~ 0.2 – 0.5 \AA). It is possible that the He II, C III, and N III lines are not of nebular origin but of stellar origin, because the effective temperature of the central star (29 300 K; Phillips 2003) is not high enough for species with an ionization potential (IP) $\gtrsim 40$ eV to exist in the nebula. For example, we did not detect any nebular lines from species with an IP $\gtrsim 40$ eV, such as [Ne III] $\lambda\lambda 3876/3967$ (IP > 41 eV) and [Ar IV] $\lambda 4711/40$ (> 40.7 eV). The IPs of He II, C III, and N III are 54.4, 47.9, and 47.5 eV, respectively.

For our analysis, we also used the emission-line fluxes in the 7700–9300 \AA range measured by Henry et al. (2010) scaled in such a way that the shorter wavelength part of their spectrum matches our HDS observations.

2.2. HST/WFPC2 archive data

⁷ IRAF is distributed by the National Optical Astronomy Observatories, which are operated by the Association of Universities for Research in Astronomy (AURA), Inc., under a cooperative agreement with the National Science Foundation.

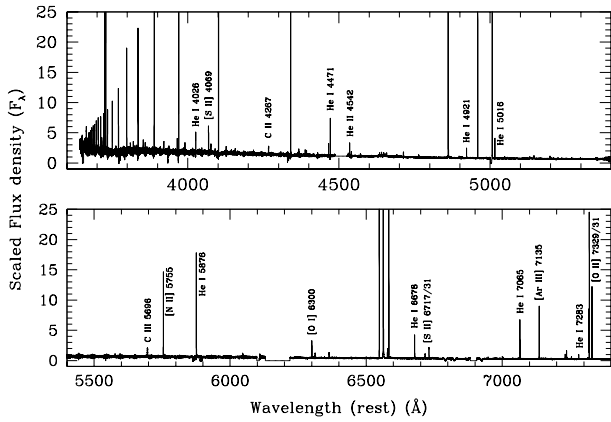


FIG. 1.— The scaled and de-reddened HDS spectrum of M1-11. The wavelength is shifted to the rest wavelength in air.

We downloaded archival *HST*/WFPC2 photometry in the F656N (6564 Å/28 Å) filter (P.I.: R.Sahai; PID: 8345), which traces the H α emission. We reduced the photometric data using the standard *HST* pipeline with MultiDrizzle, and present the drizzled M1-11 F656N image in Fig. 2. The plate scale is 0.025'' pixel⁻¹. The image shows that M1-11 is an elongated nebula; the dimensions of the bright rim are $\sim 0.8''$ along P.A. $=-27^\circ$ and $\sim 0.5''$ along P.A. $=+63^\circ$.

2.2.1. The total H α and H β fluxes

The de-reddening formula (eq. (1)) requires the total H β flux over the entire nebula to obtain the line fluxes in the *AKARI* and *Spitzer* spectra. This can be derived from the WFPC2 H α image. We find that the total flux in the F656N filter is $1.77(-11) \pm 3.48(-13)$ erg s⁻¹ cm⁻² integrated over the entire PN (we will use the notation $X(-Y)$ for $X \times 10^{-Y}$, hereafter), where we assume that the uncertainty corresponds to the standard deviation of the background. Using the HDS red spectrum and the transmission curve of the F656N filter, we estimated $\sim 12.5\%$ of the total measured flux to be due to a local continuum and the [N II] 6548 Å line flux. Thus, we estimated the solo H α line flux to be $1.55(-11)$ erg s⁻¹ cm⁻². Using the observed $F(\text{H}\alpha)/F(\text{H}\beta)$ ratio (6.57) in the HDS red spectrum, we derive the total $\log F(\text{H}\beta)$ to be -11.629 erg s⁻¹ cm⁻², which is comparable to $\log F(\text{H}\beta) = -11.84$ erg s⁻¹ cm⁻² measured by Cahn et al. (1992).

2.2.2. The hydrogen density profile

In Fig. 3(a), we present the radial profile from A toward B indicated in Fig. 2. Based on this radial profile, we examined the ionized hydrogen density $n(\text{H}^+)$ as a function of the distance from the central star R . When we restrict the integration to the optional portion of the nebula, the de-reddened observed H α flux using $c(\text{H}\beta) = 1.218$ and the reddening law of Cardelli et al. (1989) with $R_V = 3.1$, $I_l(\text{H}\alpha)$ in erg s⁻¹ cm⁻² is given by:

$$4\pi D^2 I_l(\text{H}\alpha) = \int 4\pi j(\text{H}\alpha) \epsilon dV_l, \quad (2)$$

where D is the distance to M1-11 from us; $j(\text{H}\alpha)$ is the emission coefficient; and ϵ is the filling factor which is the fraction of the nebular volume filled by ionized gas. V_l is the volume of the of the nebula. In Case B,

$$\frac{4\pi j(\text{H}\alpha)}{n(\text{H}^+)n_e} \simeq 3.856 \times 10^{-25} \left(\frac{10^4}{T_e}\right)^{-1.077}. \quad (3)$$

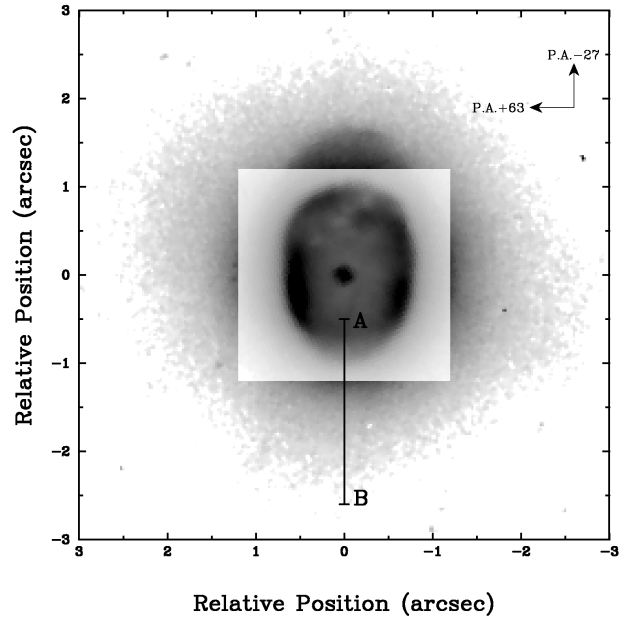


FIG. 2.— *HST*/WFPC2 F656N image of M1-11, rotated according to elongation of the nebula. In the inner 2'' \times 2'' box, the gray scale is adjusted to show the brightness of the bright rim and the central star. The radial profiles in H α and $n(\text{H}^+)$ from A (Dec. relative position $=-0.5''$) towards B ($-2.7''$) are presented in Fig. 3(a) and (b), respectively.

with $T_e = 5400$ K derived from the Balmer jump (See section 3.2), $D = 2.1$ kpc (Tajitsu & Tamura 1998), and assuming $n_e \simeq n(\text{H}^+)$, $n(\text{H}^+)$ can be written as a function of the distance from the central star R in cm as

$$n(\text{H}^+) \simeq 3.74 \times 10^{19} \left(\frac{I_l(\text{H}\alpha)}{\epsilon R}\right)^{0.5}. \quad (4)$$

The resulting $n(\text{H}^+)$ profile from A towards B with different values for ϵ is presented in Fig. 3(b). If we assume that the ionized gas is concentrated within $R = 1.0''$ and that the density has a constant value of 10^5 cm⁻³ obtained from Balmer decrements, then we find that ϵ is around 0.2. We used these $n(\text{H}^+)$ profiles with different values for ϵ in the SED modeling (See section 4.2).

2.3. ISLE Observations

We obtained J and K_s band medium-resolution ($R \sim 2500$) spectra using the near-infrared imager and spectrograph ISLE (Yanagisawa et al. 2006, 2008) attached to the Cassegrain focus of the 1.88-m telescope at the Okayama Astrophysical Observatory. The observations were done in ISLE engineering time in March 2008 (K_s) and January 2010 (J). The detector of ISLE is a 1K \times 1K HgCdTe HAWAII array. We used a science grade detector for the J -band observations and an engineering grade detector for the K_s -band observations. The entrance slit width was 1'' for both sets of observations. We fixed the P.A. at 90° during the observations. The sampling pitches in wavelength were $\sim 1.68 \times 10^{-4}$ and $\sim 3.4 \times 10^{-4}$ μm pixel⁻¹ in the J and K_s spectra, respectively, while the sampling pitch in the space direction was 0''.25 pixel⁻¹ for both spectra. We observed standard stars HIP35132 (A0V) and HIP35180 (A1V) for the J -band and HIP31900 (F0V) for the K_s -band spectra at different airmasses to calibrate the flux levels, and correct for telluric absorption and airmass extinction. We observed M1-11 in a series of 120 sec exposures in both observing modes. The total exposure times were 3600 sec

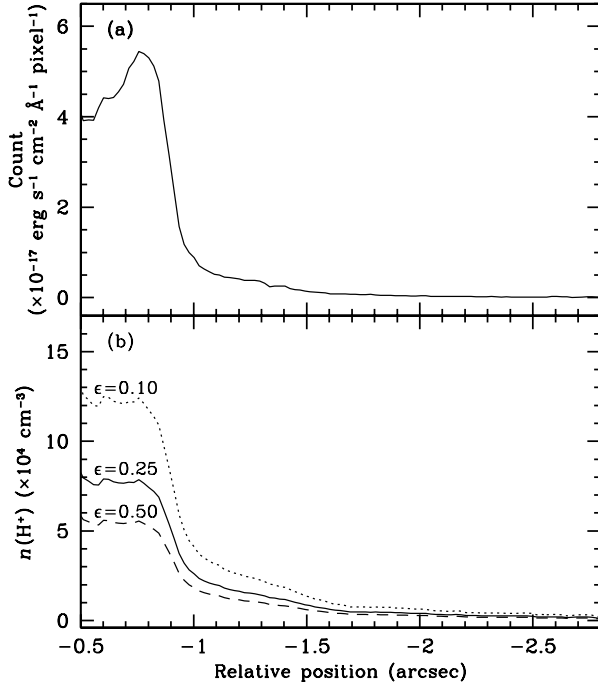


FIG. 3.— The radial profiles from A to B (Fig. 2) in $H\alpha$ (upper) and $n(H^+)$ (lower) with different filling factors ϵ .

for the J -band spectra and 3480 sec for the Ks -band spectra, respectively. Dark frames with the same science exposure time, Ar and Xe lamp frames, and on- and off-dome flat frames were also taken. For further wavelength calibration and distortion correction, OH-lines recorded in the object frames were used. The data reduction was performed in a standard manner using IRAF. The interstellar reddening corrected spectra are presented in Fig.4(a) and (b). For this correction, we adopted $c(H\beta)$ applied in the HDS red spectrum. The resulting S/Ns are >40 in the J -band and >30 in Ks -band spectra at the continuum level.

We detected more than 50 lines in these spectra, including a series of vibration-rotation excited lines of molecular hydrogen (H_2), as listed in the Appendix (Table 17). The line fluxes were normalized such that $I(Pa\beta)=100$ in the J -band and $I(Br\gamma)=100$ in the Ks -band spectra.

Fig.5 shows the spatial profiles of $Br\gamma$ and H_2 1-0 S(1)/2-1 S(1) lines in the K -band spectrum. In the both spectra, the H_2 lines are easily distinguished with other ionic lines by their spatial spread upto $\sim 16''$ in the diameter. The ratio of H_2 1-0 S(1)/2-1 S(1) is a traditional shock indicator (e.g, Hora & Latter 1994, 1996; Kelly & Hrivnak 2005). The ratio in M1-11 is ~ 4.5 at the center of the nebula, and it decreases up to ~ 1.0 outside of the ionized region. The ratio of H_2 1-0 S(1)/2-1 S(1) = 4.5 along the optical nebula ($\lesssim 6''$ in diameter) indicates a mix of UV and shock excitation (this is usual in proto-PNe, e.g., Kelly & Hrivnak 2005). Furthermore, the detection of a series of H_2 lines with upper vibrational level ($v \geq 3$) in J -band indicates that these lines are excited by fluorescence through the absorption of UV photons from the central star in photodissociation region (PDR).

The excitation diagram of H_2 lines in the entire slit of the spectra is shown in Fig.6. An ortho-to-para ratio of 3 is assumed. It clearly shows that the vibrational excitation temperature (T_{vib}) exceeds the rotation excitation temperature (T_{rot}), indicating fluorescence emission (cf. Shupe et al. 1998 for

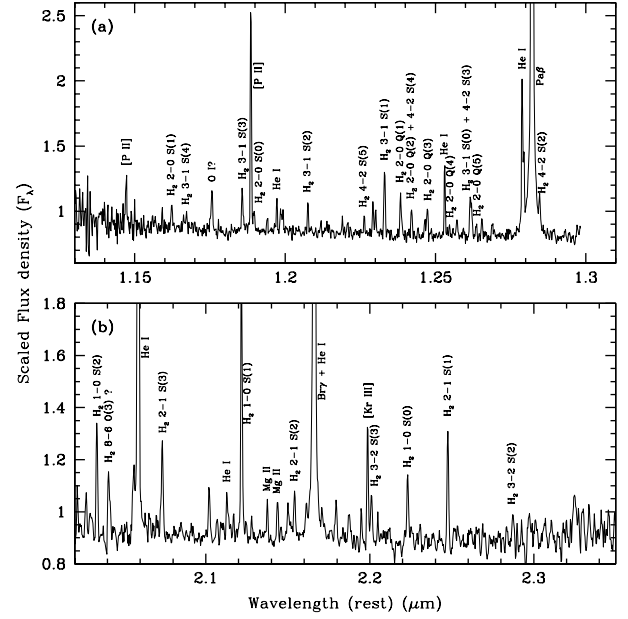


FIG. 4.— The ISLE JKs -band spectra of M1-11.

BD+30° 3639; Hora & Latter 1994 for M2-9). The difference of the excitation temperature between different rotation levels ($T_{rot} \sim 2150$ K for $v = 1$ and $T_{rot} \sim 1000$ K for $v \geq 2$) indicates H_2 lines are collisionally (shock) excited in a part (the center) of the nebula. However, it is evident that the UV excitation in PDR is still dominant for the most part of H_2 emission in M1-11.

Any pure rotational lines in *Spitzer*/IRS are not detected (see Table 2).

The lines at 1.15 and 1.19 μm are identified with [P II] (in the $^3P_1-^1D_2$ and $^3P_2-^1D_2$ transitions, respectively), representing the discovery of these lines in M1-11. Adopting the transition probabilities of Mendoza & Zeppen (1982), the collisional impacts of Tayal (2004a) and the level energy listed in Atomic Line List v2.05b12⁸, the expected [P II] $I(1.19 \mu m)/I(1.15 \mu m)$ ratio is 2.63 in $T_e=10000$ K and $n_e=5 \times 10^4 \text{ cm}^{-3}$. The observed line ratio (2.79 ± 0.44) agrees well with the theoretical value, which confirms the identification of the [P II] 1.15/1.19 μm lines. Our measurement of the $I([\text{Kr III}] 2.19 \mu m)/I(Br\gamma)$ ratio of 3.44 ± 0.23 also agrees with Sterling & Dinerstein (2008; 3.22 ± 0.26).

2.4. IUE archival data

The N^{2+} abundance can be estimated from the N III] $\lambda 1750$ line, present in archival *IUE* spectra which we retrieved from the Multi-mission Archive at the STScI (MAST). We collected low-resolution *IUE* spectra taken by the Short Wavelength Prime (SWP) and Long Wavelength Prime (LWP) cameras (file ID: SWP25846, LWP05896, and LWP05897), all of which were made using the large aperture ($10.3 \times 23 \text{ arcsec}^2$). In these spectra, we identified the He II 1640 \AA and N III] 1750 \AA lines. We determined that $c(H\beta)=0.67 \pm 0.12$, by comparing the theoretical ratio of He II $I(\lambda 1640)/(\lambda 4686)=6.56$ to the observed value, in the case of $T_e=10^4$ K and $n_e=10^4 \text{ cm}^{-3}$ as given by Storey & Hummer (1995). The interstellar extinction correction was made using equation (1). The flux measurements of the detected lines along with the normalized

⁸ see <http://www.pa.uky.edu/~peter/newpage/>

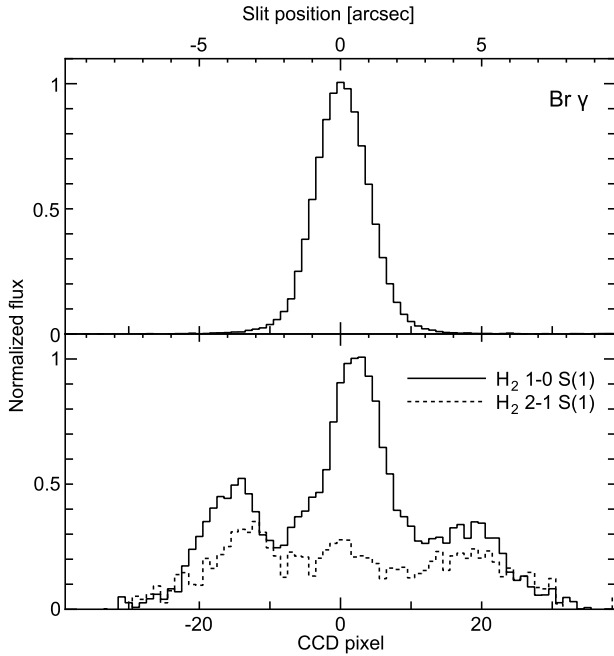


FIG. 5.— Spatial profiles of Br γ (upper panel), H₂ 1–0S(1) and 2–1S(1) lines (lower panel) along the slit in the *K*-band spectrum. After subtracted the continuum, profiles are normalized by the intensity peak of Br γ and H₂ 1–0S(1).

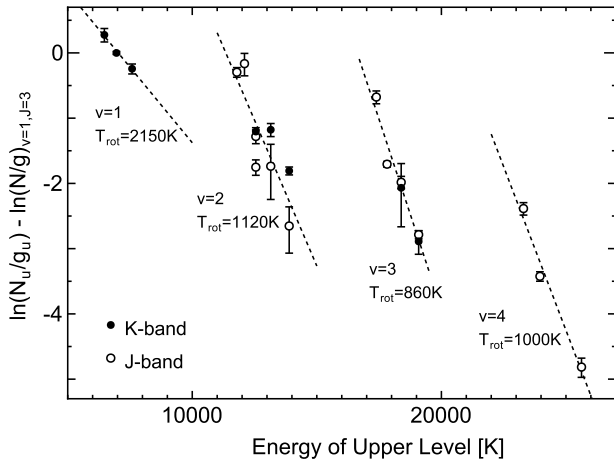


FIG. 6.— Molecular hydrogen excitation diagram from the full *J*- (open circles) and *K*-band (filled circles) spectra. Shown are the upper state vibration-rotation level populations relative to that in the $v = 1, J = 3$ level plotted against the energy of the upper state in Kelvin (K). g is the statistical weight. An ortho-to-para ratio of 3 is assumed. The points within vibrational levels fall on separate lines, as expected fluorescent-excited emission. Linear fits to the data on each vibrational level are plotted with the derived rotational temperatures.

values are listed in Table 1. While we did not detect the C III] $\lambda\lambda$ 1906/09 Å lines in the SWP and LWP spectra, Kingsburgh & Barlow (1994) show $I(\text{C III]}\lambda\lambda$ 1906/09) to be 6 with an uncertainty greater than a factor of 2.

2.5. AKARI/IRC archival data

We analyzed the 2.5–5.5 μm prism spectra of M1-11 taken with the Infrared Camera spectrograph (IRC; Onaka et al. 2007) on board of the *AKARI* satellite (Murakami et al. 2007). The data were obtained as part of a mission program, PN-SPEC (data ID: 3460037, PI: T.Onaka), on April 11, 2009. The used observing window was $1' \times 1'$. For the data reduc-

TABLE 1
LINES DETECTED IN THE *IUE* SPECTRA.

λ_{lab} (Å)	Ion	$f(\lambda)$	$F(\lambda)^a$ (erg s ⁻¹ cm ⁻²)	$I(\lambda)$ ($I(\text{H}\beta)=100$)
1640	He II	1.177	$5.03(-14) \pm 9.99(-15)$	0.51 ± 0.20
1750	N III]	1.154	$1.51(-13) \pm 1.52(-14)$	1.48 ± 0.51

^a $\log F(\text{H}\beta) = -11.63 \text{ erg s}^{-1} \text{ cm}^{-2}$.

tion, we used the IRC Spectroscopy Toolkit for the Phase 3 data version. Fig. 7 shows the IRC spectrum with a local dust continuum subtracted. The S/N is >30 for the dust continuum. Several prominent lines are visible, and their central wavelengths are indicated by dotted lines. The line fluxes are listed in Table 2. For the IRC spectra, we derived that $c(\text{H}\beta) = 1.40 \pm 0.03$ by comparing the observed intensity ratios of H I 4–5 (Br α 4.051 μm), 4–6 (Br β 2.625 μm), and 5–7 (Pf β 4.653 μm) to H β and the theoretical values of Storey & Hummer (1995) for the case of 10^4 K and 10^4 cm^{-3} . To correct for interstellar reddening, we used the ratio of the extinction at each wavelength to the $B-V$ color excess, $A_\lambda/E(B-V)$, given by Fluks et al. (1994), in combination with the correlation between H β and the color excess, $c(\text{H}\beta) = 1.47E(B-V)$, from Seaton (1979).

In the *AKARI* spectra we also found an emission band at 3.2–3.6 μm , which may be due to aromatic and aliphatic hydrocarbon species. A similar feature is seen in PN NGC 7027 and proto-PN (PPN) IRAS 21282+5050, the latter of which has a [WC11] central star. *ISO/SWS* archival spectra of NGC 7027 and IRAS 21282+5050 are shown for reference in Fig. 7. The resonance at 3.3 μm is attributed to vibrational transitions in polycyclic aromatic hydrocarbons (PAHs; e.g. Draine 2011). We also recognize the 6.2, 7.7, and 11.3 μm resonances due to PAHs in the spectra of M1-11. In particular, the 11.3 μm C-H out-of-plane bending mode is seen in the *Spitzer*/IRS spectrum (See next section). Cohen et al. (1986) already detected the 6.2, 6.7, 7.7, and 8.6 μm resonances in M1-11. The 3.3 μm band profile of M1-11 is similar to the ones seen in NGC 7027 and IRAS 2182+5050, and thus we assume that the emission seen in M1-11 is also due to PAHs. Indeed, the 3.3 μm feature was first detected by Allen et al. (1982), who also measured its flux. Using the theoretical intensity ratio of H I $I(5-9)$ to $I(5-11) = 1.86$ in the case of $T_e = 10^4 \text{ K}$ and $n_e = 10^4 \text{ cm}^{-3}$, we removed the contribution from H I $n=5-9$ to the 3.3 μm feature and estimated the flux due to PAHs $I(\text{PAH } 3.3 \mu\text{m})$ to be $7.63(-12) \text{ erg s}^{-1} \text{ cm}^{-2}$, which is about twice as large as the measurement by Allen et al. (1982; $3.1(-12) \text{ erg s}^{-1} \text{ cm}^{-2}$).

2.6. Spitzer/IRS and VLT/VISIR archival data

M1-11 was observed by *Spitzer* on November 10, 2006 with the 9.9–19.6 μm (SH) and 18.7–37.2 μm (LH) modes on the Infrared Spectrograph (IRS, Houck et al. 2004), as part of program ID 30430 (PI: H. Dinerstein; AORKEY: 19903232). We downloaded the archival spectral images, and after masking bad pixels using IRSCLEAN, we extracted the one-dimensional spectra using SPICE. The S/N is >30 for the dust continuum.

In the spectrum of Cohen et al. (1986), very weak and tentative features are seen around 7.0 and 8.5 μm that may arise at least partially from fullerene C₆₀ with possible blending from the PAH 8.5 μm band. However, the quality of their data is insufficient to be confident of these features. To check the

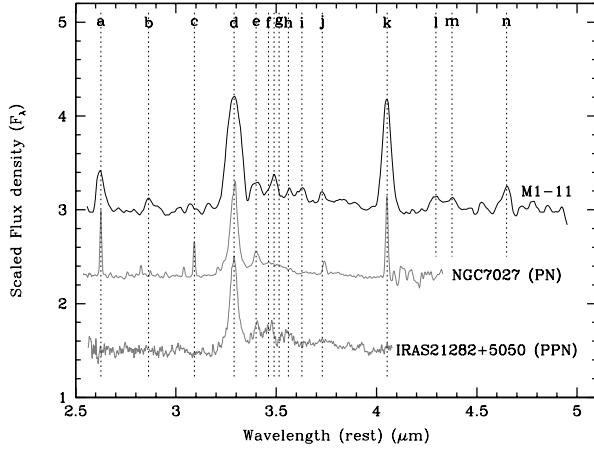


FIG. 7.— Comparison of the AKARI/IRC spectrum of M1-11 (upper line), the archival ISO/SWS spectra of the PN NGC7027 and the PPN IRAS21282+5050 (middle & lower). The identified lines are indicated by the broken lines. The IDs are indicated by lower case letters; a: Br β 2.63 μm ; b: H I 5-11 2.86 μm ; c: PAH 3.29 μm C-H stretch + H I 5-9 3.29 μm ; d: PAH 3.38/3.40 μm asymmetric CH₃, CH₂ stretch; e: PAH 3.46 μm lone C-H stretch; f: PAH 3.49/3.51 μm symmetric CH₃, CH₂ stretch; g: PAH 3.56 μm aldehydes C-H stretch; h: H I 6-19,20 3.63 μm ; j: Br α 4.05 μm ; k: H I 4-5,6-14 4.05 μm ; l: He I 3-5 4.30 μm ; m: H I 6-12 4.38 μm ; n: Pf β 4.65 μm (Reference of the wavelength of the hydrocarbon lines: Kwok 2007).

TABLE 2
DETECTED LINES IN THE AKARI/IRC, *Spitzer*/IRS, AND VLT/VISIR OBSERVATIONS.

λ_{vac} (μm)	Ion	$f(\lambda)$	$F(\lambda)^a$ ($\text{erg s}^{-1} \text{cm}^{-2}$)	$I(\lambda)$ ($I(\text{H}\beta)=100$)
2.63	H I (Br β)	-0.955	2.09(-12) \pm 2.32(-13)	4.1 \pm 0.5
2.86	H I 5-11	-0.962	6.12(-13) \pm 8.41(-14)	1.2 \pm 0.2
3.29	PAH + H I 5-9	-0.971	8.81(-12) \pm 2.55(-13)	16.2 \pm 1.0
3.41	PAH	-0.973	1.47(-12) \pm 2.98(-13)	2.7 \pm 0.6
3.49	PAH	-0.974	2.04(-12) \pm 3.77(-13)	3.7 \pm 0.7
3.56	PAH	-0.975	6.92(-13) \pm 3.47(-13)	1.3 \pm 0.6
3.63	H I 6-19 + H I 6-20	-0.976	1.59(-12) \pm 4.08(-13)	2.9 \pm 0.8
3.73	H I 5-8	-0.977	1.06(-12) \pm 4.58(-13)	1.9 \pm 0.8
3.82	H I 6-16	-0.978	1.19(-12) \pm 8.38(-13)	2.1 \pm 1.5
3.91	H I 6-15	-0.979	6.25(-13) \pm 5.40(-13)	1.1 \pm 1.0
4.05	H I (Br α) + H I 6-14	-0.980	4.94(-12) \pm 7.94(-14)	8.9 \pm 0.5
4.30	He I 3-5	-0.982	6.97(-13) \pm 6.52(-14)	3.1 \pm 1.4
4.38	H I 6-12	-0.982	5.72(-13) \pm 7.07(-14)	1.0 \pm 0.1
4.65	H I (Pf β) + H I 6-11	-0.984	8.99(-13) \pm 1.17(-13)	1.6 \pm 0.2
8.5	C ₆₀ ^b	-0.970	3.66(-12) \pm 4.59(-13)	6.8 \pm 0.9
8.6	PAH ^c	-0.970	5.10(-12) \pm 5.07(-13)	9.4 \pm 1.0
8.99	[Ar III]	-0.959	1.60(-12) \pm 1.75(-13)	3.1 \pm 0.4
12.37	H I 6-7,8-11	-0.980	9.68(-13) \pm 4.24(-14)	1.0 \pm 0.1
12.71	He I	-0.982	4.85(-13) \pm 5.35(-14)	0.5 \pm 0.1
12.81	[Ne II]	-0.983	2.90(-11) \pm 4.35(-13)	30.9 \pm 1.5
17.3	C ₆₀ ^d	-0.981	4.61(-12) \pm 4.78(-13)	4.9 \pm 0.6
18.71	[S III]	-0.981	1.31(-12) \pm 7.27(-14)	1.4 \pm 0.1
18.9	C ₆₀ ^e	-0.981	6.88(-12) \pm 2.55(-13)	7.4 \pm 0.4
33.16	He I	-0.993	1.47(-12) \pm 2.57(-13)	1.5 \pm 0.3
35.83	He I	-0.993	3.89(-12) \pm 2.85(-13)	4.0 \pm 0.3

NOTE. — For interstellar reddening correction, we used $c(\text{H}\beta)=1.403\pm 0.025$ for the AKARI/IRC and 1.629 ± 0.020 for the *Spitzer*/IRC spectra, respectively.

^a $\log F(\text{H}\beta) = -11.63 \text{ erg s}^{-1} \text{cm}^{-2}$.

^b The FWHM is 0.17 μm .

^c The sum of two Gaussian components representing the PAH 8.6 μm . See text in detail.

^d The FWHM is $0.51\pm 0.04 \mu\text{m}$.

^e The FWHM is $0.36\pm 0.03 \mu\text{m}$.

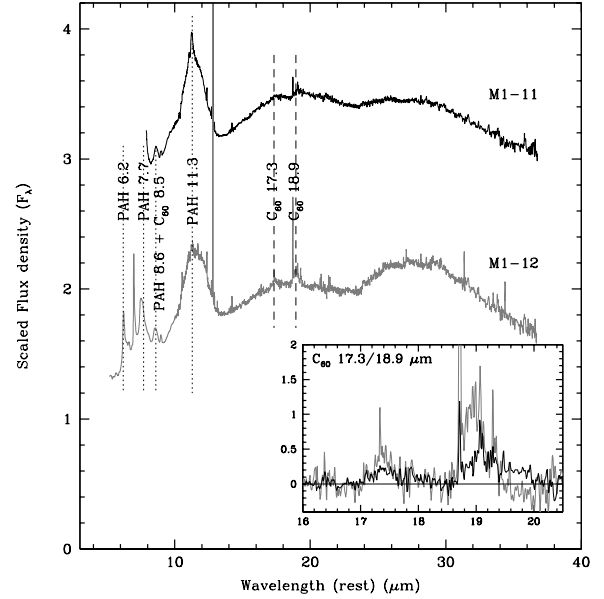


FIG. 8.— The *Spitzer* spectra of M1-11 (black line) and M1-12 (gray line). (inner box) The line-profiles of C₆₀ 17.33 and 18.94 μm . The line-profiles of C₆₀ at 8.5 μm in M1-11 and M1-12 are present in Fig.10.

presence of the C₆₀ 8.5 μm feature, we downloaded the 7.7-13.3 μm archival spectral data obtained using the VLT spectrometer and imager for the mid-infrared (VISIR) at ESO VLT UT3 (ID: 084.D-0868A; PI: E.Lagadec). We reduced the raw data using ESO *gasgano*. To compare the VISIR data with the *Spitzer* spectra of other C₆₀ PNe and also to combine it with the M1-11's *Spitzer* spectrum, we degraded the original VISIR spectral resolving power of ~ 400 down to 90 by using a Gaussian convolution technique. The S/N of the convoluted VISIR spectrum is >70 .

The IRS and VISIR combined 7.7-37.2 μm spectrum which is shown in Fig. 8, reveals the solid-state/molecular features and atomic lines on the dust continuum thermal emission. The detected lines are listed in Table 2. The emission around 8.5 μm is the complex of C₆₀ 8.5 μm and PAH 8.6 μm . We measured the flux density of C₆₀ 8.5 μm by using multiple Gaussian fitting to separate its flux from the PAH 8.6 μm feature (See section 2.6.3). We performed the interstellar reddening correction in a similar way as described in Section 2.5. By comparing the observed intensity ratios H I $F(n=6-7)/F(\text{H}\beta)$ & $F(n=8-11)/F(\text{H}\beta)$ to the theoretical values of Storey & Hummer (1995) for the case B assumption in $T_e=10^4$ K and $n_e=10^4 \text{ cm}^{-3}$, we derived that $c(\text{H}\beta)=1.63\pm 0.02$.

2.6.1. Broad spectral features at 10–13 and 16–22 μm

M1-11 appears to have C-rich dust, as evidenced by the presence of a broad 10-13 μm feature, which is usually attributed to SiC in the literature. This feature (centered around 11.3 μm) is seen on top of a featureless continuum, presumably due to amorphous carbon (AC). The PAH features around 10–11 μm are also visible in the spectrum. A second broad feature is seen around approximately 16–22 μm , similar in appearance to broad features reported in several PNe in the Magellanic Clouds (Stanghellini et al. 2007; Bernard-Salas et al. 2009; García-Hernández et al. 2011a; García-Hernández et al. 2012)

While Stanghellini et al. (2007) associate this emission feature with carbon-rich dust, Bernard-Salas et al. (2009) show that the 16–22 μm broad feature differs from the PAH plateau

TABLE 3
C AND O ABUNDANCES DERIVED FROM CELS, FOR MAGELLANIC
CLOUD PNE SHOWING THE 16–22 μm FEATURE.

Nebula	C ^a	O ^a	C/O	Ref.
SMC1	8.11	8.26	0.71	(1)
SMC6	8.03	8.22	0.65	(1)
LMC8	7.93	8.26	0.47	(2)
LMC25	8.29	8.17	1.32	(3),(4)
LMC48	8.40	8.24	1.45	(3),(4)
LMC85	8.74	8.40	2.19	(2)

REFERENCES. — (1) Idiart et al. (2007); (2) Dopita et al. (1997); (3) Stanghellini et al. (2005); (4) Leisy & Dennefeld (2006)

^a The number density relative to the hydrogen is defined as log H=12.

around 16–20 μm (Van Kerckhoven et al. 2000) and the 21 μm feature sometimes seen in carbon-rich post-AGB stars (e.g. Volk et al. 2011) and PNe (Hony et al. 2001), and is more similar to the 18 μm amorphous silicate feature, thus assigning a oxygen-rich carrier for this feature in objects. Bernard-Salas et al. (2009) imply that if the silicate identification for this feature is correct, the Magellanic Cloud PNe often show a dual dust chemistry, although earlier in the same study they state that not a single source in their sample shows a mixed chemistry, thus undermining the silicate identification of the 16–22 μm bump. Indeed, in a comprehensive study of a large sample of Galactic and Magellanic Cloud PNe, Stanghellini et al. (2012) conclude that none of the LMC PNe considered show a dual chemistry, lending more credibility to the idea that the 16–22 μm feature is carried by a carbon-based material.

Considering the gas chemistry adds to the confusion. Table 3 shows the C and O gas-phase abundances derived from the CELs for six of the PNe with 16–22 μm emission features discussed by Bernard-Salas et al. (2009) and García-Hernández et al. (2011a). Three of the six are O-rich in their gas-phase material, while the remaining three MC PNe actually show a C-rich chemistry. Since the C abundances of SMC1 and SMC6 have relatively large uncertainty (0.25 dex), these two SMC PNe could be C-rich. Even with this information, it remains unclear whether the 16–22 μm bump is due to an O-rich or a C-rich carrier. Thus we do not assign any identification to this feature, and do not include fitting the 16–22 μm bump in our analysis.

2.6.2. 30 μm broad feature

The carrier of the 30 μm feature remains somewhat of a mystery. While MgS has been proposed and often used as the carrier of this feature (Hony et al. 2003), recent work has cast doubt on the identification with MgS (see e.g., Zhang et al. 2009; García-Hernández et al. 2010; Zhang & Kwok 2011). Nevertheless, we consider MgS as a possible dust component in M1-11 to explain the 30 μm feature in the spectrum.

Other potential carriers, in particular hydrogenated amorphous carbon (HAC) (see Grishko et al. 2001; Hony et al. 2003), should also be considered. In the SED model for proto-PN HD 56126, Hony et al. (2003) showed that broad emission features around 7–9 μm and 10–13 μm are partly due to HACs, making the identification of the 30 μm band with HACs (Grishko et al. 2001), a possibility. We examined whether HAC can be the main contributor to the 10–13 and 30 μm broad features by applying a modified blackbody model to the IRS spectrum, including both MgS and HACs.

The observed flux density F_λ due to thermal emission from

TABLE 4
ADOPTED OPTICAL CONSTANTS FOR EACH MODEL DUST COMPONENT.

Dust species	Data source
SiC	Pegourie (1988)
amorphous carbon (AC)	Rouleau & Martin (1991)
MgS	Begemann et al. (1994)
HAC	Hony et al. (2003)

dust grains is given by

$$F_\lambda = \sum_i \left(\frac{4}{3} \pi a_i \rho_i D^2 \right)^{-1} m_{d,i} Q_{\lambda,i} \pi B_\lambda(T_{d,i}), \quad (5)$$

where a_i is the grain radius of component i , ρ_i is the dust density, $m_{d,i}$ is the dust mass, $Q_{\lambda,i}$ is the absorption efficiency, and $B_\lambda(T_{d,i})$ is the Planck function for a dust temperature $T_{d,i}$. We adopt a distance $D = 2.1$ kpc (Tajitsu & Tamura 1998). In Table 4 we list the optical constants that we use for each of the dust species considered. For MgS, we used the optical constants of nearly pure MgS, e.g. Mg_{0.9}Fe_{0.1}S, from Begemann et al. (1994). For the HACs, we adopt the Q_λ of HAC in the case of H/(H+C)=0.3 calculated by Hony et al. (2003). In two models, we consider different compositions, consisting of combinations of PAHs, amorphous carbon (AC), SiC, MgS, and HAC (Fig. 9). We considered 9.9–37.2 μm *Spitzer* spectrum and *AKARI* FIS 65/90 μm photometry data, except for the 16–22 μm broad band. We assume spherically shaped grains with a radius of $a=0.5$ μm for AC, SiC, and HACs, and we excluded PAHs. To reproduce the broad 30 μm emission using MgS, as discussed in Hony et al. (2003), we considered a continuous distribution of ellipsoids (CDE, e.g., Bohren & Huffman 1983; Fabian et al. 2001; Min et al. 2003) and calculated Q_λ of CDE MgS using Eq. 18 given by Min et al. (2003). To simplify, we assume that the value of each ellipsoid MgS grain is $\simeq 4\pi a^3/3$, where a is 0.5 μm .

The results of the modified blackbody fitting is shown in Fig. 9, and the derived $T_{d,i}$, $m_{d,i}$, and mass fraction for each dust component are summarized in Table 5. Model 1 with AC, SiC, and MgS can explain the observed spectrum reasonably well, while the model 2 with HAC instead of MgS predicts an unseen broad emission feature around 20 μm . However, we should keep in mind that it is extremely difficult to characterize carbon compounds with a mixed aromatic and aliphatic content - such as HACs - in the laboratory because these optical constants are strongly variable for different chemical and physical conditions. Jones (2012) presents HAC theoretical models that show the extreme variability of HAC spectra depending on parameters such as hydrogen-content, grain size, etc. In any case, the 20 μm feature is much weaker than the 30 μm feature (see Ghrisko et al. 2001) and one could detect the 30 μm features while not detecting the 20 μm feature. At present, therefore, we do not completely rule out that HACs as a carrier of the 30 μm broad feature.

In this paper, therefore, we assume that SiC and MgS are the main contributors to the 10–13 and 30 μm broad features, respectively. In the remainder of our analysis, we will only consider PAHs, SiC, AC, and MgS to model the dust emission in the SED.

2.6.3. 8.5, 17.3, and 18.9 μm emission due to C₆₀ fullerenes

In the VISIR and *Spitzer* combined spectrum of M1-11, we see infrared features at 8.5 (although blended with the PAH

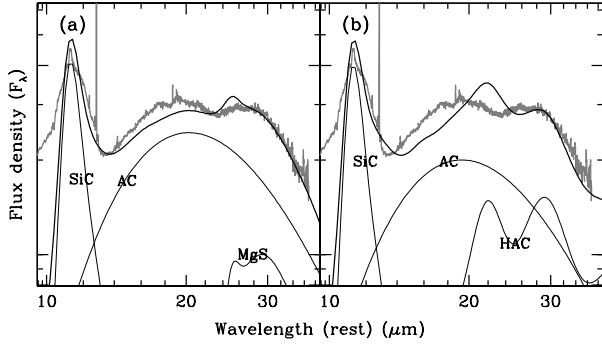


FIG. 9.— The observed *Spitzer*/IRS and VLT/VISIR spectrum of M1-11 (gray lines) and the predicted SED from modified blackbody fitting (thick lines). Each component is indicated by a thin line. AC stands for amorphous carbon.

TABLE 5
RESULTS FROM THE MODIFIED BLACKBODY FITTING TO THE
Spitzer/IRS SPECTRUM.

Models	Dust Comp.	T_d (K)	m_d (M_\odot)
model 1 (Fig.9a)	SiC	160	2.85(-5)
	AC	120	2.97(-4)
	MgS	220	3.17(-6)
model 2 (Fig.9b)	SiC	170	1.75(-5)
	AC	120	1.77(-4)
	HAC	80	0.11

8.6 μm , see below), 17.3, and 18.9 μm , most likely due to the fullerene C_{60} .

In our own Milky Way Galaxy, these C_{60} infrared features were recently detected in five PNe, including Tc1, M1-12, M1-20, K3-54, and M1-60 (Cami et al. 2010; García-Hernández et al. 2010; García-Hernández et al. 2012), a C-rich PPN (IRAS01005+7910; Zhang & Kwok 2011), and two O-rich post-AGB stars (IRAS06338+5333 and HD52961; Gielen et al. 2011). In Fig.8, we show the IRS spectrum of M1-12 in comparison to M1-11. The C_{60} 17.3 and 18.9 μm features seem to be present in M1-11 although they are much weaker than those in M1-12. The spectrum of M1-12 shows spectral features due to PAHs, SiC, AC, MgS, and a very weak 16–22 μm feature, which resembles that of M1-11. The 16–22 μm feature is not seen in Tc1, M1-20, K3-54, and M1-60. Some other PNe with fullerenes in the Magellanic Clouds exhibit the 16–22 μm feature (García-Hernández et al. 2011a; García-Hernández et al. 2012). In the inset of Fig.8, the \sim 16–20 μm spectra of M1-11 and M1-12 with a local dust continuum subtracted, are shown. The wavelength positions of the intensity peak and the line widths of C_{60} 17.3 and 18.9 μm lines in M1-11 are almost coincident with those in M1-12. In addition, the complex line around 8.5–8.6 μm - which turns out to be a blend of PAH 8.6 μm and C_{60} 8.5 μm - in M1-11 is very similar to that in M1-12, as shown in Fig. 10. These comparison with M1-12 supports the identification of this feature as a C_{60} +PAH blend.

To quantify the excitation temperature and the total number of C_{60} , we need to separate flux of C_{60} 8.5 μm from the PAH 8.6 μm band. Cami et al. (2010) reported that the FWHM of C_{60} 8.5 μm in the PN Tc1 is 0.15 μm by Gaussian fitting. Tc1 shows strong C_{60} lines but very weak PAH bands. Assuming that the FWHM of C_{60} 8.5 μm is \sim 0.15 μm in M1-11 and M1-12, we fit the broad line at 8.6 μm with multiple Gaussians.

The line at 8.6 μm in M1-11 can be represented by three plus one Gaussian components, as shown in Fig.10a. We assume that the profile of the PAH 8.6 μm line is represented by the sum of two Gaussians at the peak wavelengths of \sim 8.7 and \sim 8.8 μm . The FWHM of the PAH 8.6 μm represented by the sum of these two Gaussian is 0.2 μm , which is consistent with NGC7027 (0.23 μm in ISO/SWS spectrum shown in Fig. 7). The FWHM of the C_{60} 8.5 μm line indicated by the blue line is 0.17 μm . The FWHM of the C_{60} and PAH complex is 0.3 μm . The resultant Gaussian fitting for M1-12 is presented in Fig.10b. The PAH 8.6 μm is represented by the sum of two Gaussians at \sim 8.6 and \sim 8.7 μm . The FWHMs of the C_{60} and the PAHs for M1-12 are as same as those of M1-11. The measured fluxes of the C_{60} 8.5 μm and PAH 8.6 μm lines in M1-11 are listed in Table 2.

The excitation temperature and the number of C_{60} were derived by creating a vibration excitation diagram as shown in Fig.10c. We followed the method of Cami et al. (2010). N_u is the number of C_{60} molecules in the upper vibrational levels. N_u is written by

$$N_u = \frac{4\pi I(C_{60})D^2}{A} \frac{\lambda}{hc}, \quad (6)$$

where $I(C_{60})$ is the fluxes of C_{60} lines in $\text{erg s}^{-1} \text{cm}^{-2}$, D is the distance to M1-11 (2.1 kpc; Tajitsu & Tamura 1998), A are the transition probabilities (4.2, 1.1, 1.9 s^{-1} for C_{60} 8.5, 17.3, and 18.9 μm , respectively, from García-Hernández et al. 2011b), h is Planck's constant, and c is the speed of light. The vibrational degeneracy is given by g_u . In thermal equilibrium, the Boltzmann equation relates the N_u to the excitation temperature T_{ext} :

$$N_u \propto g_u \exp(-Eu/kT_{ext}). \quad (7)$$

Eu and k are the energy of the excited level and the Boltzmann constant, respectively. We confirmed that our measured excitation temperature, T_{ext} of 338 ± 9 K in Tc 1 using Eqs. (6) and (7) is consistent with Cami et al. (2010; 332 K). Accordingly, we obtained T_{ext} of 399 ± 36 K and the $N(C_{60})$ of $4.57 \pm 1.23(+46)$. The total mass of C_{60} m_{C60} is $2.75(-8) M_\odot$.

Our estimated T_{ext} , $N(C_{60})$, and m_{C60} in M1-12 are 345 ± 35 K, $5.30 \pm 1.23(+46)$, and $3.18(-8) M_\odot$, respectively, adopting D of 3.9 kpc (Tajitsu & Tamura 1998). García-Hernández et al. (2010) measured the T_{ext} in M1-12 of 546 K. Their measured FWHM of C_{60} 8.5 μm is 0.237 μm . The T_{ext} discrepancy between theirs is due to the differences in the measured line flux of this line.

3. RESULTS

3.1. CELs plasma diagnostic

We determined the electron temperatures T_e and densities n_e using 11 diagnostic CELs, and listed the results in Table 7.

For [N II] λ 5755 and [O II] $\lambda\lambda$ 7320/30, we subtracted the recombination contamination from both lines using

$$\frac{I_R([\text{NII}]\lambda 5755)}{I(\text{H}\beta)} = 3.19 \left(\frac{T_e}{10^4} \right)^{0.33} \times \frac{\text{N}^{2+}}{\text{H}^+}, \quad (8)$$

and

$$\frac{I_R([\text{OII}]\lambda\lambda 7320/30)}{I(\text{H}\beta)} = 9.36 \left(\frac{T_e}{10^4} \right)^{0.44} \times \frac{\text{O}^{2+}}{\text{H}^+}. \quad (9)$$

given by Liu et al. (2000). Adopting N^{2+} and O^{2+} ionic abundances derived from N II and O II lines (see Section 3.4), we

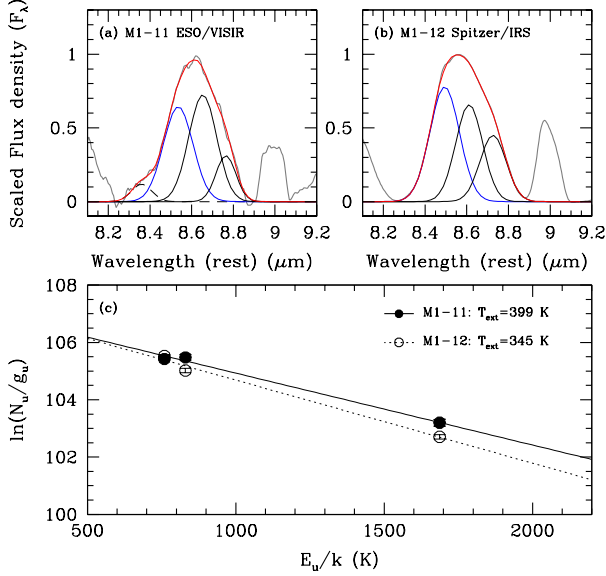


FIG. 10.— (panels (a) and (b)) The line-profiles of C₆₀ at 8.5 μm in M1-11 and M1-12 (blue lines). The local dust continua are subtracted. The gray lines are the observations. We fit the broad line at 8.6 μm by three or four Gaussian. The deconvolved profiles are indicated by the black and blue lines. The red lines are the sum of these components. The emission-line around 9 μm is [Ar III] 8.99 μm . (panel (c)) The excitation diagram for C₆₀ in M1-11 and M1-12. The filled and open circles are the observed data in M1-11 and M1-12, respectively. The lines indicated represent the best fit to the data. See text in detail.

derived that $I_R([\text{N II}] \lambda 5755) = 0.12$ and $I_R([\text{O II}] \lambda 7320/30) = 2.11$. The recombination contamination is $\sim 2\%$ in [N II] $\lambda 5755$ and $\sim 8\%$ in [O II], respectively.

The resulting n_e - T_e diagnostic diagram is shown in Fig. 11. The solid lines indicate diagnostic lines for the electron temperatures, while the broken lines are electron density diagnostics. Since the gas in M1-11 has much higher density than the critical densities of the density sensitive lines [O II] $\lambda\lambda 3726/29$ and [S II] $\lambda\lambda 6717/31$, the ratios of [O II] $I(\lambda\lambda 3726/29)/I(\lambda\lambda 7320/30)$ and [S II] $I(\lambda\lambda 6717/31)/I(\lambda\lambda 4069/76)$ are density-sensitive rather than temperature-sensitive. The critical densities at $T_e = 10\,000$ K for [O II] $\lambda\lambda 3726/29$ are ~ 4500 and ~ 980 cm^{-3} , respectively, and those of [S II] $\lambda\lambda 6717/31$ are ~ 1400 and ~ 3600 cm^{-3} , respectively. The densities derived from the [O II] $\lambda\lambda 3726/29$ and [S II] $\lambda\lambda 6717/31$ ratios might be the value for thin shell region, while those from the [O II] $I(\lambda\lambda 3726/29)/I(\lambda\lambda 7320/30)$ and [S II] $I(\lambda\lambda 6717/31)/I(\lambda\lambda 4069/76)$ would be the value for the bright rim. To determine n_e , we adopted $T_e = 10\,000$ K for all density-diagnostic lines. $T_e([\text{N II}])$ was calculated using $n_e = 36\,490$ cm^{-3} , which is the average between $n_e([\text{O II}])$ derived from $I(\lambda\lambda 3726/29)/I(\lambda\lambda 7320/30)$ ($n_e([\text{O II}]_{n/a}$) hereafter) and $n_e([\text{S III}])$. For $T_e([\text{S III}])$, $T_e([\text{O III}])$, and $T_e([\text{Ar III}])$, we adopted $n_e([\text{S III}])$. For $T_e([\text{O I}])$, we adopted $n_e([\text{N I}])$. Our estimates for $T_e([\text{N II}])$, $T_e([\text{O III}])$, and $T_e([\text{S III}])$ are in excellent agreement with those by Henry et al. (2010), who estimated 10 720, 9996, and 9100 K, respectively. The estimates for n_e and T_e are summarized in Table 7.

To calculate the CEL ionic abundances, we adopt a three zone model based on n_e - T_e diagram. The T_e and n_e combinations for each ion are listed in Table 6. For the N⁰ and O⁰ abundances, we adopted $T_e([\text{O I}])$ and $n_e([\text{N I}])$ (zone 1). The averaged n_e is from $n_e([\text{O II}]_{n/a})$ and $n_e([\text{S III}])$; and $T_e([\text{N II}])$

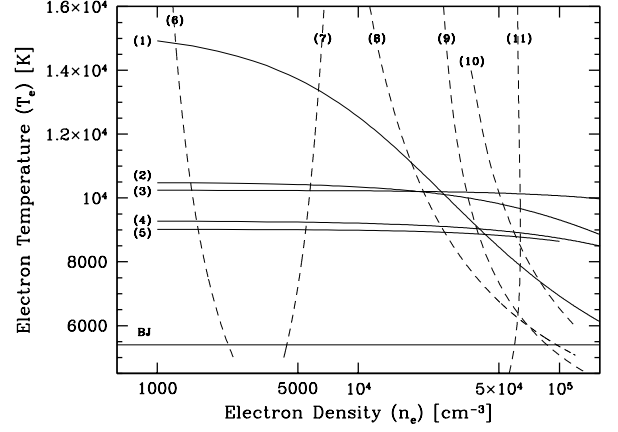


FIG. 11.— n_e - T_e diagram. Each curve is labeled with an ID number given in Table 7. The solid lines indicate diagnostic lines of the T_e . The broken lines indicate diagnostic lines of the n_e .

TABLE 6
ADOPTING n_e AND T_e FOR THE CEL IONIC ABUNDANCE CALCULATIONS.

Zone	Ions	n_e (cm^{-3})	T_e (K)
1	N ⁰ , O ⁰	1380	9240
2	N ⁺ , O ⁺ , P ⁺ , S ⁺ , Cl ⁺	36 490	8410
3	O ²⁺ , Ne ⁺ , S ²⁺ , Cl ²⁺ , Ar ²⁺ , Fe ²⁺ , Kr ²⁺	51 120	9540

is for ions with $0 < \text{IP} \lesssim 13.6$ eV (zone 2). $n_e([\text{S III}])$ and the averaged temperature among $T_e([\text{O III}])$, $T_e([\text{S III}])$, and $T_e([\text{Ar III}])$ is for ions with I.P. = 14.4–35.5 eV (zone 3).

3.2. RL plasma diagnostics

We calculate the He, C, N, and O abundances using RLs of these elements by adopting the T_e derived from the Balmer discontinuity together with He I line ratios and the n_e from the Balmer decrements, listed in Table 7. The Balmer discontinuity temperature $T_e(\text{BJ})$ was determined using the method described by Liu et al. (2001), which we used to obtain the C²⁺, N²⁺, and O²⁺ abundances from recombination lines.

The He I electron temperatures $T_e(\text{He I})$ were derived from the ratios of He I $I(\lambda 7281)/I(\lambda 6678)$, $I(\lambda 7281)/I(\lambda 5876)$, and $I(\lambda 6678)/I(\lambda 5876)$ assuming a constant electron density of 10^6 cm^{-3} , estimated from the Balmer decrements (see below). We adopted the emissivities of He I by Benjamin et al. (1999). The $T_e(\text{He I})$ derived from three different line ratio combinations is 3980–6980 K. We adopted $T_e(\text{He I})$ derived from He I $I(\lambda 7281)/I(\lambda 6678)$ for the He⁺ abundance calculations. The reason why this $T_e(\text{He I})$ is the most reliable was discussed in Otsuka et al. (2010).

The intensity ratios of the high-order Balmer lines H_n (n : the principal quantum number of the upper level) to a lower Balmer line, e.g., H β , are also sensitive to the electron density. In Fig. 12, we plot the ratios of higher-order Balmer lines to H β compared to the theoretical values by Storey & Hummer (1995) for $T_e(\text{BJ})$ and n_e of 10^5 , 5×10^5 , and 10^6 cm^{-3} . The electron density in the recombination line emitting regions seems to be $> 10^5$ cm^{-3} . Care when dealing with this value is necessary, because it apparently has large scatter.

3.3. CEL ionic abundances

TABLE 7
 PLASMA DIAGNOSTIC RESULTS.

	ID	Diagnostic	Value	Result	
T_e (K)	(1)	[N II] ($\lambda 6548/83$)/($\lambda 5755$)	42.45 ± 1.14^a	8410 ± 90	
	(2)	[O III] ($\lambda 4959/5007$)/($\lambda 4363$)	182.94 ± 20.32	9740 ± 330	
	(3)	[Ar III] ($\lambda 7135$)/($\lambda 5192$)	132.44 ± 26.92	$10\,060 \pm 780$	
	(4)	[O I] ($\lambda 6300/63$)/($\lambda 5577$)	74.62 ± 14.31	9240 ± 640	
	(5)	[S III] ($\lambda 9069$)/($\lambda 6313$)	9.96 ± 2.63	8830 ± 980	
		He I ($\lambda 7281$)/($\lambda 6678$)	0.20 ± 0.01	6890 ± 330	
		He I ($\lambda 7281$)/($\lambda 5876$)	0.052 ± 0.002	5920 ± 230	
		He I ($\lambda 6678$)/($\lambda 5876$)	0.26 ± 0.01	3980 ± 160	
		Average		5600	
		BJ	Balmer Jump		5400 ± 1300
	n_e (cm^{-3})	(6)	[N I] ($\lambda 5198$)/($\lambda 5200$)	1.63 ± 0.13	1380 ± 350
(7)		[O II] ($\lambda 3726$)/($\lambda 3729$)	2.75 ± 0.05	5750 ± 380	
(8)		[O II] ($\lambda 3626/29$)/($\lambda 7320/30$)	3.11 ± 0.10^b	$21\,860 \pm 780$	
(9)		[S II] ($\lambda 6716/31$)/($\lambda 4069/76$)	0.63 ± 0.02	$35\,350 \pm 1400$	
(10)		[S III] ($\lambda 18.71 \mu\text{m}$)/($\lambda 9069$)	0.44 ± 0.11	$51\,120 \pm 15\,550$	
(11)		[Cl III] ($\lambda 5517$)/($\lambda 5537$)	0.40 ± 0.10	$22\,110\text{--}63\,730$	
		Balmer decrements		$10^2\text{--}10^6$	

^a Corrected recombination contribution for [N II] $\lambda 5755$.

^b Corrected recombination contribution for [O II] $\lambda \lambda 7320/30$.

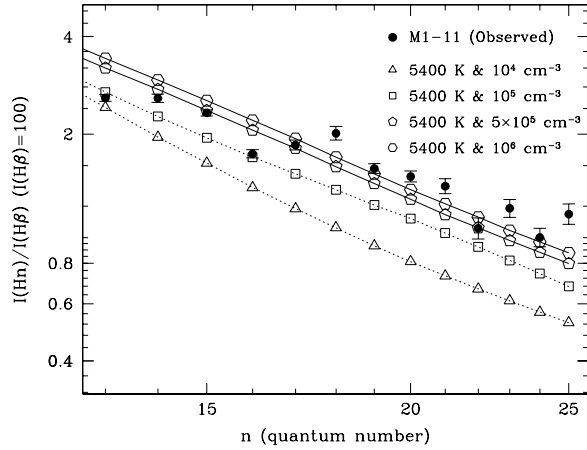


FIG. 12.— Plot of the intensity ratio of the higher order Balmer lines to $H\beta$ (Case B assumption) with the theoretical intensity ratios in $T_e=5400$ K and different n_e .

The derived ionic abundances are listed in Table 8. In the last line of the transition series for each ion, we present the adopted ionic abundance in bold face. The adopted values represent the line intensity weighted mean in case two or more lines are detected. As references, the results by Sterling & Dinerstein (2008, for Kr) and Henry et al. (2010, for the others) are also listed in the last column. This is the first time the Ne^+ , P^+ , and Fe^{2+} abundances are derived for M1-11. In total, fifteen ionic abundances are determined by solving for a >5 level atomic model, with the exception of Ne^+ , for which the abundance was calculated using a two level energy model. We adopted the same collisional strengths and transition probabilities used in Otsuka et al. (2010, 2011) except for Cl^+ , for which we adopted the transition probabilities from the CHIANTI atomic database⁹, the collisional impacts of Tayal (2004b), and the level energy listed in Atomic Line List v2.05b12. We subtracted the recombination contamination in the [N II] $\lambda 5755$ and [O II] $\lambda \lambda 7320/30$ lines to derive the N^+ and O^+ abundances.

In general, our derived abundances are comparable to the values of Henry et al. (2010) and Sterling & Dinerstein

(2008). The discrepancies between our N^+ , O^+ , S^+ abundances and the results by Henry et al. (2010) are mainly due to adopted electron temperature; Henry et al. adopted 10 200 K. Note that they employed three different T_e s and a constant $n_e=20\,000 \text{ cm}^{-3}$ in their models. With their T_e s, we would find N^+ , O^+ , and S^+ abundances comparable to their results. Lastly, a minor discrepancy for the N^+ and O^+ abundances must be due to the recombination contamination in the [N II] $\lambda 5755$ and [O II] $\lambda \lambda 7320/30$ lines, respectively.

3.4. RL ionic abundances

Our values for the ionic abundances derived from RLs are listed in Table 9. In general, the Case B assumption applies to lines from levels having the same spin as the ground state, and the Case A assumption applies to lines of other multiplicities. In the last of the line series of each ion, we present the adopted ionic abundance and the error estimated from the line intensity-weighted mean. Effective recombination coefficients for the lines' parent multiplet are the same as those used by Otsuka et al. (2010). The RL ionic abundances are insensitive to the electron density under $\lesssim 10^8 \text{ cm}^{-3}$ (Zhang & Liu 2003). For the ionic abundance calculations, we therefore adopted the effective recombination coefficients in case of $n_e=10^4 \text{ cm}^{-3}$ for C^{2+} and N^{2+} . For He^+ and O^{2+} calculations, we adopted $n_e=10^6 \text{ cm}^{-3}$ and 10^4 cm^{-3} , respectively. Since He II, C III, C IV, N III, and O III appeared to be of stellar origin, we did not estimate the abundances of these ions.

The He^+ abundances are determined using electron density insensitive six He I lines to reduce intensity enhancement by collisional excitation from the $\text{He}^0 2s \ ^3S$ level. For the C^{2+} abundances, the V6 and V17.06 lines, which have higher angular momentum as upper levels, seem to be unaffected by both resonance fluorescence by starlight and recombination from excited 2S and 2D terms. Comparison of the C^{2+} abundances derived from V6 and V17.06 lines indicated that the observed C II lines would have less population enhancement mechanisms. Our estimated He^+ and C^{2+} abundances are consistent with Henry et al. (2010; 3.56(−), 4.48(−)).

We estimated the O^{2+} abundances using the O II lines showing the least contamination from other ionic transitions. We excluded the O II 4676.23 Å line when determining O^{2+} abundance, because this line is much stronger than the other V1

⁹ <http://www.ukssdc.ac.uk/solar/chianti/>

TABLE 8
IONIC ABUNDANCES DERIVED FROM CELS.

X^{m+}	λ_{lab} (Å or μm)	$I(\lambda)$ [$I(\text{H}\beta)=100$]	X^{m+}/H^+	Others	
N ⁰	5197.90	2.01(-1) ± 9.10(-3)	3.25(-7) ± 7.79(-8)	...	
	5200.26	1.23(-1) ± 7.78(-3)	3.21(-7) ± 7.54(-8)	...	
N ⁺	5754.64	5.87(0) ± 1.08(-1)	1.14(-4) ± 6.93(-6)	4.32(-5)	
	6527.24	3.02(-2) ± 4.27(-3)	7.25(-5) ± 1.05(-5)	...	
	6548.04	5.89(+1) ± 9.89(-1)	8.41(-5) ± 3.08(-6)	4.13(-5)	
	6583.46	1.90(+2) ± 4.77(0)	9.18(-5) ± 3.77(-6)	4.32(-5)	
			9.05(-5) ± 3.68(-6)	4.28(-5)	
N ²⁺	1750	1.48(0) ± 5.08(-1)	3.10(-5) ± 1.85(-5)	...	
O ⁰	5577.34	3.95(-2) ± 7.56(-3)	5.87(-6) ± 2.39(-6)	...	
	6300.30	2.20(0) ± 4.08(-2)	5.79(-6) ± 1.34(-6)	3.26(-6)	
	6363.78	7.48(-1) ± 2.13(-2)	6.15(-6) ± 1.43(-6)	3.57(-6)	
O ⁺	3726.03	5.54(+1) ± 5.26(-1)	3.87(-4) ± 2.12(-5)	6.27(-5) ^d	
	3728.81	1.97(+1) ± 3.02(-1)	5.02(-4) ± 2.83(-5)	...	
	7320/30	2.37(+1) ± 6.92(-1)	3.40(-4) ± 2.67(-5)	7.15(-5)	
O ²⁺	4361.21	1.37(-1) ± 1.52(-2)	8.83(-6) ± 3.50(-6)	5.77(-6)	
	4958.91	6.44(0) ± 3.09(-2)	8.27(-6) ± 1.81(-6)	5.44(-6)	
	5006.84	1.85(+1) ± 8.17(-2)	8.25(-6) ± 1.80(-6)	5.77(-6)	
Ne ⁺	12.81	3.09(+1) ± 1.45(0)	4.76(-5) ± 2.98(-6)	...	
	P ⁺	1.15	1.22(-1) ± 1.82(-2)	2.19(-8) ± 3.30(-9)	...
	1.19	3.41(-1) ± 1.54(-2)	2.32(-8) ± 1.14(-9)	...	
S ⁺	4068.60	1.79(0) ± 4.65(-2)	4.49(-7) ± 2.19(-8)	...	
	4076.35	6.34(-1) ± 5.55(-2)	4.74(-7) ± 4.58(-8)	...	
	6716.44	4.42(-1) ± 1.61(-2)	3.63(-7) ± 1.72(-8)	1.30(-7)	
	6730.81	1.08(0) ± 2.68(-2)	4.15(-7) ± 1.62(-8)	1.46(-7)	
			4.34(-7) ± 2.37(-9)	1.41(-7)	
S ²⁺	6312.10	3.23(-1) ± 1.50(-2)	8.45(-7) ± 2.23(-7)	7.67(-7)	
	9068.60	3.22(0) ± 7.49(-1)	1.02(-6) ± 2.73(-7)	...	
	18.71	1.40(0) ± 1.00(-1)	9.59(-7) ± 9.04(-8)	...	
Cl ⁺	8578.69	1.19(-1) ± 2.62(-2)	8.11(-9) ± 1.80(-9)	7.68(-7)	
	9123.60	7.76(-2) ± 2.74(-2)	2.03(-8) ± 7.18(-9)	1.29(-8)	
			1.29(-8) ± 3.92(-9)	1.29(-8)	
Cl ²⁺	5517.66	2.88(-2) ± 5.72(-3)	1.51(-8) ± 4.15(-9)	...	
	5537.60	7.22(-2) ± 1.15(-2)	1.55(-8) ± 3.85(-9)	...	
			1.54(-8) ± 3.94(-9)	...	
Ar ²⁺	5191.82	1.86(-2) ± 3.76(-3)	2.91(-7) ± 1.07(-7)	...	
	7135.80	2.46(0) ± 4.18(-2)	2.20(-7) ± 2.51(-7)	3.90(-7)	
	8.99	3.06(0) ± 3.76(-1)	4.38(-7) ± 5.85(-8)	...	
Fe ²⁺	4701.53	6.89(-2) ± 8.46(-3)	9.31(-8) ± 2.28(-8)	1.86(-7)	
	4754.69	3.86(-2) ± 8.65(-3)	1.26(-7) ± 3.90(-8)	...	
	4769.43	5.32(-2) ± 6.12(-3)	2.08(-7) ± 5.03(-8)	...	
	4881.00	4.93(-2) ± 5.38(-3)	3.74(-8) ± 9.27(-9)	...	
	4934.08	1.63(-2) ± 3.54(-3)	1.49(-7) ± 4.42(-8)	...	
	5270.40	7.06(-2) ± 3.70(-3)	8.20(-8) ± 1.63(-8)	...	
Kr ²⁺	2.19	8.84(-2) ± 7.28(-3)	3.52(-9) ± 3.87(-10)	2.99(-9)	

NOTE. — (in fifth column) All values except for Kr²⁺ are from Henry et al. (2010). The Kr²⁺ abundance is from Sterling & Dinerstein (2008).

^a Based on [O II] $\lambda\lambda 3726/29$ complex.

lines.

The abundance discrepancy factor (ADF), which is the ratio of RL to CEL abundances, is 19.5 ± 8.4 for O²⁺ and 15.3 ± 13.6 for N²⁺. The large uncertainty of ADF(N²⁺) is due to the large uncertainty in the CEL N²⁺ abundance. ADF(O²⁺) in M1-11 is comparable to that of high density PN M2-24 (namely, 17; Zhang & Liu 2003). Zhang & Liu (2003) also found that the density structure for M1-11 and M2-24 is similar, with M2-24 showing a large density contrast of $n_e = 10^{3-6} \text{ cm}^{-3}$.

TABLE 9
IONIC ABUNDANCES DERIVED FROM RLS.

X^+	Multi.	λ_{lab} (Å)	$I(\lambda)$ [$I(\text{H}\beta)=100$]	X^{m+}/H^+
He ⁺	V11	5876.66	6.16(0) ± 8.32(-2)	4.17(-2) ± 2.93(-3)
	V14	4471.47	1.72(0) ± 3.02(-2)	3.37(-2) ± 1.98(-3)
	V45	7281.35	3.19(-1) ± 1.27(-2)	3.60(-2) ± 2.74(-3)
	V46	6678.16	1.60(0) ± 2.78(-2)	3.83(-2) ± 1.97(-3)
	V48	4921.93	4.64(-1) ± 7.25(-3)	3.38(-2) ± 1.99(-3)
C ²⁺	V51	4387.93	2.38(-1) ± 8.44(-3)	3.78(-2) ± 2.99(-3)
	V2	6578.01	4.99(-1) ± 1.25(-2)	3.93(-2) ± 2.58(-3)
	V3	7231.33	2.16(-1) ± 1.25(-2)	6.76(-4) ± 3.11(-4)
	V3	7236.42	4.36(-1) ± 1.08(-2)	5.13(-4) ± 2.26(-4)
	V3	7237.17	7.14(-2) ± 4.99(-3)	5.77(-4) ± 2.52(-4)
N ²⁺	V6	4267.15	6.14(-1) ± 2.68(-2)	8.44(-4) ± 3.74(-4)
	V17.06	5342.43	3.20(-2) ± 4.30(-3)	5.31(-4) ± 2.00(-4)
	V3	5666.63	1.01(-1) ± 4.80(-2)	5.37(-4) ± 2.42(-4)
	V3	5677.66	5.18(-2) ± 1.00(-2)	5.59(-4) ± 2.31(-4)
	V5	4630.54	5.49(-2) ± 7.05(-3)	5.09(-4) ± 3.61(-4)
O ²⁺	V19	5017.22	1.38(-2) ± 3.58(-3)	5.51(-4) ± 3.09(-4)
	V1	4641.81	2.61(-2) ± 1.01(-3)	2.74(-4) ± 1.46(-4)
	V1	4676.23	8.59(-2) ± 6.78(-3)	5.12(-4) ± 3.07(-4)
	V1	4649.14	2.20(-2) ± 6.00(-3)	4.61(-4) ± 2.92(-4)
	V1	4650.84	3.10(-2) ± 7.00(-3)	1.52(-4) ± 4.68(-5)
			9.22(-4) ± 1.19(-4)	1.17(-4) ± 4.80(-5)
			2.00(-4) ± 7.59(-5)	1.61(-4) ± 5.85(-5)

3.5. Elemental abundances

The elemental abundances are estimated using an ionization correction factor, ICF(X), based on the IP. ICFs(X) for each element are listed in Table 10. The He abundance is the sum of the He⁺ and He⁰⁺ abundances, and we allowed for the unseen He⁰ abundance. The C abundance is the sum of the C⁺ and C²⁺ abundances, and we added the unseen C⁺ using ICF(C). Henry et al. (2010) used ICF(C)=O/O²⁺. Since the IPs of C^{+,2+} (11.3 and 24.4 eV) are close to those of N^{+,2+} (14.5 and 29.6 eV), we instead adopted ICF(C)=N/N²⁺. The N abundance is the sum of N⁺ and N²⁺. For the RL N abundance, we corrected for the unseen N⁺ assuming $(N/N^{2+})_{\text{CEL}} = (N/N^{2+})_{\text{RL}}$. The O abundance is the sum of the O⁺ and O²⁺ abundances. For the RL O abundance, we assume $(O^{2+}/O)_{\text{RLs}} = (O^{2+}/O)_{\text{CELS}}$. The Ne abundance is equal to the Ne⁺ abundance. The P abundance is the sum of the P⁺ and P²⁺ abundances. We assumed that P/P⁺ = S/S⁺ and considered the P²⁺ abundance. The S abundance is the sum of the S⁺, S²⁺, and S³⁺ abundances. We corrected for the unseen S³⁺ abundance using the CEL O and O⁺ abundances. We assume that the Cl abundance is the sum of Cl⁺ and Cl²⁺. The Ar abundance is the sum of the Ar⁺ and Ar²⁺ abundances, and we corrected for the unseen Ar⁺. The Fe abundance is the sum of the Fe²⁺ and Fe³⁺ abundances, and we corrected for the unseen Fe³⁺. The Kr abundance is the sum of the Kr⁺, Kr²⁺ and Kr³⁺ abundances, and we corrected for the unseen Kr⁺ and Kr³⁺.

The resulting elemental abundances are listed in Table 11. The types of emission lines used for the abundance estimations are specified in the second column. The number densities of each element relative to hydrogen are listed in the third column, and the subsequent two columns are the number densities in the form of $\log_{10}(X/H)$, where H is 12, and the relative number densities to the solar value. The last columns are the measurements by Sterling & Dinerstein (2008) for Kr and Henry et al. (2010) for the others. Our estimated abundances are in agreement with the values given by these authors except for C, N, and O. The C discrepancy between Henry

TABLE 10
ADOPTED IONIZATION CORRECTION FACTORS (ICFs).

X	Type	ICF(X)	X/H
He	RL	S/S ²⁺	ICF(He)He ⁺
C	RL	(N/N ²⁺) _{CEL}	ICF(C)C ²⁺
N	CEL	1	ICF(N)(N ⁺ +N ²⁺)
	RL	(N/N ²⁺) _{CEL}	ICF(N)N ²⁺
O	CEL	1	ICF(O)(O ⁺ +O ²⁺)
	RL	(O/O ²⁺) _{CEL}	ICF(O)O ²⁺
Ne	CEL	1	ICF(Ne)Ne ⁺
P	CEL	(S/S ⁺)	ICF(P)P ⁺
S	CEL	[1 - (1 - (O ⁺ /O)) ³] ^{-1/3}	ICF(S)(S ⁺ +S ²⁺)
Cl	CEL	1	ICF(Cl)(Cl ⁺ +Cl ²⁺)
Ar	CEL	(N/N ²⁺) _{CEL}	ICF(Ar)Ar ²⁺
Fe	CEL	(O/O ⁺)	ICF(Fe)Fe ²⁺
Kr	CEL	Cl/Cl ²⁺	ICF(Kr)Kr ²⁺

TABLE 11
ELEMENTAL ABUNDANCES OF M1-11.

X	Type	X/H	log(X/H)+12	[X/H] ^a	Others
He	RL	5.65(-2)±7.36(-3)	10.75±0.06	-0.15±0.06	10.55
C	RL	2.19(-3)±1.60(-3)	9.34±0.32	+0.95±0.41	9.78
N	CEL	1.22(-4)±1.85(-5)	8.08±0.07	+0.25±0.13	7.67
	RL	1.81(-3)±1.58(-3)	9.26±0.38	+1.43±0.60	...
O	CEL	4.13(-4)±2.40(-5)	8.62±0.03	-0.07±0.06	7.88
	RL	8.05(-3)±3.45(-3)	9.91±0.19	+1.22±0.21	...
Ne	CEL	4.76(-5)±2.98(-6)	7.68±0.03	-0.19±0.10	...
P	CEL	7.51(-8)±8.59(-9)	4.88±0.06	-0.58±0.06	...
S	CEL	1.43(-6)±9.34(-8)	6.15±0.03	-1.04±0.05	5.96
Cl	CEL	2.83(-8)±5.56(-9)	4.45±0.09	-0.81±0.11	4.11
Ar	CEL	9.85(-7)±6.15(-7)	5.99±0.27	-0.81±0.11	5.37
Fe	CEL	1.13(-7)±2.97(-8)	5.05±0.11	-2.42±0.12	...
Kr	CEL	6.48(-9)±2.21(-9)	3.81±0.15	+0.53±0.17	4.25

^a The solar abundances are from Lodders (2003).

et al. (2010) and ours is due to the different ICF(C). When we assume ICF(C)=O/O²⁺, we find that the C abundance is 10.45±0.22. The N and O discrepancies are due to the N⁺ and O⁺ discrepancies caused by the differently adopted T_e 's.

4. DISCUSSION

4.1. C and O abundances and the C/O abundance ratio

We attempted to estimate the carbon abundance from CELs by correlating ADF(C²⁺) with ADF(O²⁺). We found a tight correlation, ADF(C²⁺)=0.997×ADF(O²⁺), among 56 Galactic PNe from Wang & Liu (2007), Wesson et al. (2005), Liu et al. (2004), and Tsamis et al. (2004). When we consider only the 18 PNe with ADF(O²⁺)>5, there seems to be no correlation between ADF(C²⁺) and ADF(O²⁺). For these 18 PNe ADF(C²⁺) is 7.65±1.97. When we adopt this value for ADF(C²⁺), the C²⁺ abundance derived from CELs is 7.31(-5)±3.56(-5) and the I(C III)λ1906/09 is 33.8±16.5. The CEL C abundance and the CEL C/O ratio are 8.46±0.34 dex and -0.14±0.34 dex, respectively. The CEL C/O ratio derived from CELs agrees well with the value derived from RLs, which is -0.57±0.37 dex, although there is a large uncertainty.

We should keep in mind that the >9 dex C abundances derived from both the CELs and the RLs are confirmed in many PNe and can also be theoretically explained by AGB nucleosynthesis if we assume a small minimum H-envelope mass for the third dredge-up (~0.5 M_⊙; Straniero et al. 1997 for solar metallicity). However, for stars with a main sequence

TABLE 12
COMPARISON OF THE OBSERVED ABUNDANCES WITH THE PREDICTION BY AN INITIALLY 1.5 M_⊙ STAR WITH Z=0.004 (SEE TEXT IN DETAIL).

He	C	N	O	Ne	P	Sources
10.75	9.34/8.46	8.08	8.62	7.68	4.88	This work
10.97	8.46	7.65	8.23	7.42	4.86	Karakas (2010)

mass of ~1-3 M_⊙ and an initial metallicity of Z=0.004, O abundances of >9 dex are not expected to occur. For example, we present the predicted abundances for initially 1.5 M_⊙ stars with in Table 12. In M1-11, we adopt the observed N and O abundances derived from CELs, while for the C abundances we used CEL *predictions* and observed values for the RLs. Karakas (2010) adopted scaled-solar abundances as the initial composition. The accuracy of the predicted abundances is within 0.3 dex. The model predicted C and O abundances are close to the *predicted* CEL C and the observed CEL O abundances. The model could also explain the observed abundance of Ne and P, which are He-rich intershell products that are brought up to the stellar surface by the third dredge-up in late AGB phase.

Comparison of the model of Karakas (2010) and our observation suggests that the CEL O abundance would be more reliable in M1-11 relative to the RL O. This would be also applied to the N abundance. Therefore, we consider the CEL CNO abundances to represent the gas-phase abundances of these elements in M1-11. If the CEL C/O ratio is correct, M1-11 might be a C-rich or O-rich PN. In the next section, we verify the C and O abundances through gas+dust SED modeling.

4.2. SED modeling

We investigate the fractional ionization, the evolutionary stage of the central star, and the physical conditions of the ionized gas and dust grains, by constructing an SED model based on the photo-ionization (P-I) code CLOUDY c08.00 and modified blackbody fitting. Through SED modeling, we derive the ionized gas mass m_g , dust mass m_d , and dust temperature T_d in the nebula, as well as the total luminosity L_* and the effective stellar temperature T_{eff} . We verify CEL C and O abundances through our model.

4.2.1. Model approach

Using CLOUDY and modified blackbody fitting, we attempted to fit the observed SED from ~0.1 to 90 μm, assuming that the dust in M1-11 is composed of PAHs, amorphous carbon (AC), SiC, and MgS grains. We excluded the broad 16-22 μm feature in the fitting procedure.

Since there are no optical constants of MgS available for the UV, we could not include MgS in the CLOUDY modeling. Instead, we fitted the MgS feature using single temperature thermal emission applied to the infrared opacity. For MgS, we assumed CDE, while for all other dust species we used spherical grains. Unfortunately, CLOUDY does not allow CDE grains, providing a second reason to model the MgS contribution separately. Indeed, at present, there are no publicly available P-I codes which can handle CDE grain shapes.

We assume that the observed SEDs can be expressed as the sum of the calculated SED from the CLOUDY model and the modified blackbody fit to the MgS emission. First, we fitted the SED in the range from ~0.1 to 22.5 μm and 65-90 μm using CLOUDY. Then, we fitted a modified blackbody to the

difference between the observations and the fitted SED from CLOUDY, to account for the contribution from MgS. In both the CLOUDY model and the MgS modified blackbody fitting, we adopted a distance D to M1-11 of 2.1 kpc.

In the CLOUDY calculations, we used Tlusty's non-LTE theoretical atmosphere model¹⁰ with $[Z/H]=-0.81$, which is consistent with the observed $[Ar/H]$. McCarthy et al. (1997) found that the effective temperature $T_{\text{eff}}=29\,000$ K, the surface gravity $\log g=3.0$, and the core mass $M_*=0.74 M_{\odot}$ for the central star, using their non-LTE model based on Keck/HIRES spectra. However, they adopted a distance D of 4.6 kpc. Guided by their results, we used a series of theoretical atmosphere models with T_{eff} in the range from 27 500 to 35 000 K and $\log g$ values of 3.0, 3.25, 3.50, 3.75, and 4.0 to describe the SED of the central star. We found that $T_{\text{eff}}=31\,950$ K, $\log g=3.5$, and a total luminosity $L_*=4510 L_{\odot}$ can accommodate the observations well.

For the gas-phase elemental abundances X/H , we adopted the observed values listed in Table 11 as a first guess and varied these to match observations, except for C. For C, we varied the C abundance to match the predicted value: $I(C\text{ III})\lambda 1906/09=33.8\pm 16.5$. We did not fit the He II, C III or N III lines, because these lines would be of stellar wind origin. For the N abundances, we adopted the CEL value. Treating the collisional impacts of [P II] as a function of electron temperature and solving the 5-level energy model for this ion is not included in CLOUDY c08.00, leading to an overestimate of the P abundance ($\log_{10} P/H + 12 > 6$). We adapted the code to perform this analysis correctly, and obtain a better estimate of the P abundance. We also revised the C III], [N II], [O II, III], [Ne II], [S III], and [Ar III] line-calculation programs in CLOUDY. The abundance of elements that were not observed was fixed at $[X/H]=-0.81$. Reliable dielectric recombination (DR) rate measurements do not exist for low stages of ionization of S at photo-ionization temperatures (CLOUDY c08 manual), thus we adopted the scaled DR of oxygen for sulfur line calculations, to match the observed [S II].

We adopted the hydrogen density profile as presented in Fig. 3(b). Based on the *HST* image shown in Fig. 2, we fixed the outer radius R_{out} at $2.6''$ (0.026 pc) and varied the inner radius R_{in} and filling factor ϵ to match the observed SED. The best fit R_{in} and ϵ are $\sim 0.8''$ (0.008 pc) and 0.25-0.3, respectively, assuming that the gas and dust co-exist in the same sized nebula.

We assumed that amorphous carbon and SiC are present in the form of spherical dust grains with a radius $a=0.5 \mu\text{m}$. To calculate the opacities for these species, we used the optical constants listed in Table 4. Zhang & Kwok (1990) observed a near IR-excess, also shown in the SED of Fig. 13, arising from both the PAH and the small dust grain emission. To explain the excess, we also included small carbonaceous grains with a grain size of $a=0.005 \mu\text{m}$, as well as PAHs. We adopted the optical data of Desert et al. (1990), Schutte et al. (1993), and Bregman et al. (1989). To explain the MgS feature around $30 \mu\text{m}$, we performed a modified blackbody fitting with a single dust temperature T_d and CDE shaped grains with a characteristic size of $a=0.5 \mu\text{m}$ as we mentioned in Section 2.6.2.

To verify the degree of modeling accuracy, we evaluated the gas emission line strengths and the broad band fluxes in the features of interest (Table 14), including three *AKARI/FIS* and two Wide-field Infrared Survey Explorer (*WISE*) photometry bands; and we fitted the overall SED shape with the adopted

elemental abundances. We will discuss the resulting elemental abundance and the ionization correction factors.

4.2.2. Results of SED modeling

The derived physical quantities are listed in Tables 13 and 14, which can be compared with the flux levels in the 13 spectral features of interest. In Table 14, we compare the predicted emission line and band fluxes with the observed values, where $I(H\beta)$ is 100 and the intrinsic $\log I(H\beta)$ is $-10.22 \text{ erg s}^{-1} \text{ cm}^{-2}$. Columns 4 and 5 list the observed values and the values predicted by CLOUDY modeling. The type of emission is indicated in column 3.

The predicted CEL C and O abundances are close to the model results by Karakas (2010). The predicted CEL C/O ratio (+0.19 dex) suggests that M1-11 could be a normal low-mass C-rich PN slowly evolving toward higher effective temperatures. The elemental abundances predicted by CLOUDY are comparable with the observation and are in excellent agreement with the model prediction by Karakas (2010).

In Fig. 13, we present the calculated SED from CLOUDY (dots), the MgS modified blackbody fitting (broken line), and the sum of those two components (thick line). The gray lines and circles represent the observations including the *IUE* spectra, 2MASS *JHKs* (Ramos-Larios & Phillips 2005), the *AKARI* 9/18/65/90 μm , and the *WISE* 3 and 4 μm photometry. In the inset, we focus on the $\sim 10\text{-}40 \mu\text{m}$ part of the SED. The predicted SED matches the data in UV to mid-IR range well, except for the PAH emission, in particular the $13.6 \mu\text{m}$ feature due to the C-H out of plane bending mode (quartet).

The temperatures of the $0.5\text{-}\mu\text{m}$ sized amorphous carbon, SiC, and MgS are 91, 102 (by CLOUDY), and 160-200 K (by blackbody fitting), respectively. The temperature of the $0.005\text{-}\mu\text{m}$ sized amorphous carbon grains and PAHs are 177 K and 267 K, respectively. The gas C mass within $2.6''$ predicted by CLOUDY is $4.68(-5) M_{\odot}$. Most of the C in the nebula is existing as the grains. The mass of pure C₆₀ in the nebula is only $\sim 0.008\%$ of the total C dust.

Assuming a distance of 2.1 kpc, the initial mass of the progenitor is estimated to be $1\text{-}1.5 M_{\odot}$ based on the location of M1-11 with respect to the post-AGB H-burning evolutionary tracks with $Z = 0.004$ (Vassiliadis & Wood 1994), as shown in Fig. 14. The age is > 1000 yrs after leaving the AGB phase.

4.3. Fullerene formation in PNe

Since the discovery of fullerenes C₆₀ and C₇₀ in a C-rich PN Tc1 (Cami et al. 2010), the number of detections of these lines are increasing (García-Hernández et al. 2010, 2011a; Zhang & Kwok 2011); however, the formation process of fullerenes in evolved stars and in the ISM is under debate. At present three explanations for fullerene formation are proposed.

4.3.1. Destruction of HAC

García-Hernández et al. (2010) suggested that PAHs and fullerenes may be formed by the photochemical processing of HAC in H-rich circumstellar envelopes. In laboratory experiments, Scott et al. (1997) showed that PAHs and C₅₀, C₆₀, and C₇₀ may be produced by the decomposition of HACs. This fullerene formation scenario seems to be supported by the *Spitzer* observations of H-poor R Coronae Borealis (RCB) stars (García-Hernández et al. 2011b) In particular, the mid-IR spectrum of the R Coronae Borealis star V854 Cen - an H-rich RCB star - evolved from HACs (*ISO/SWS* spectrum in 1996) to PAHs and C₆₀ (*Spitzer/IRS* in 2007). The *ISO/SWS*

¹⁰ <http://nova.astro.umd.edu/Tlusty2002/tlusty-frames-cloudy.html>

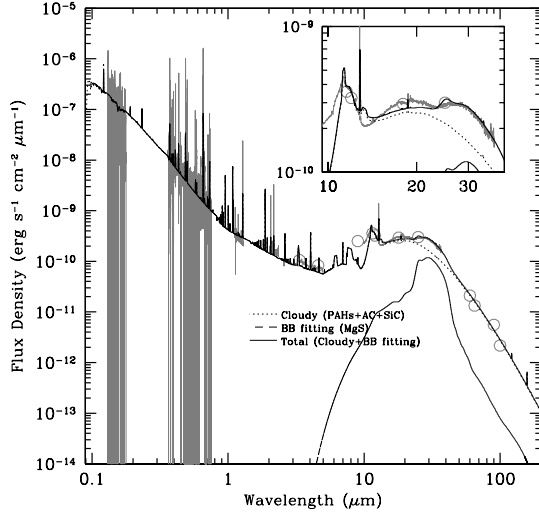


FIG. 13.— The fitted SED from the CLOUDY modeling (dots) and the modified blackbody fitting (long dash) and the resultant SED (thick black line). The gray circles and lines are data from *IUE*, Subaru/HDS, OAO/ISLE spectra, 2MASS (Ramos-Larios & Phillips 2005), *AKARI*/IRC spectra and 4 bands (9/18/65/90 μm), and *Spitzer*/IRS spectrum. In the CLOUDY model, we considered PAHs, amorphous carbon (AC), and SiC. The modified blackbody fitting is performed for MgS only. The close-up feature of the observed and fitted SEDs around 10–40 μm are presented in the inner box. See main text for a detailed description.

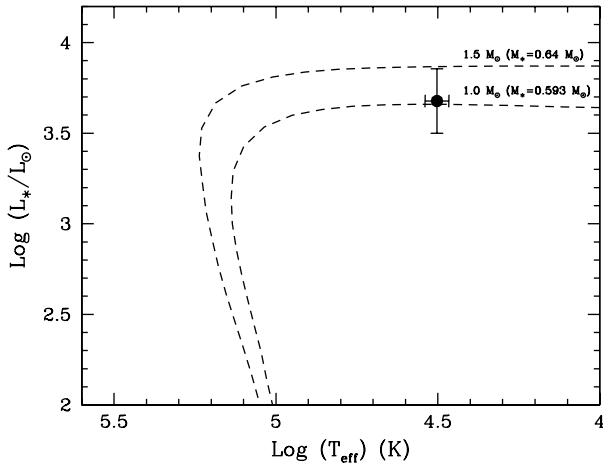


FIG. 14.— The location of M1-11 on the 1.0 and 1.5 M_{\odot} hydrogen burning evolutionary tracks after AGB phase. The location of M1-11 is indicated by the filled circle.

spectrum of this object is similar to a laboratory spectrum of HAC at 773 K (Lambert et al. 2001). Later, García-Hernández et al. (2011a) show that seven Magellanic Cloud PNe have broad features around 6–9 and 10–14 μm . The central stars of these PNe are H-rich. The 6–9 μm broad feature is different from PAH features in the same wavelength range and is rather similar to that of HACs. These MC PNe have cool central stars (31 300–43 300 K, meaning young PNe), and their UV spectra, except for SMP SMC13 and LMC2, show P-Cygni profiles, suggesting the presence of a stellar wind. This suggests that the shocks may be triggering the HAC decomposition and forming both fullerenes and PAHs. More recently, in the strong C_{60} PNe Tc1, SMC16, and LMC56, which are showing HAC features, Bernard-Salas et al. (2012) argued that the UV radiation from the central star is photochemically processing the HACs to produce fullerenes, by comparing be-

TABLE 13
THE DERIVED PROPERTIES OF THE CENTRAL STAR, IONIZED NEBULA,
AND DUST BY THE SED MODEL.

Parameters	Central Star
L_*	4710 L_{\odot}
T_{eff}	31 830 K
$\log g$	3.5 cm s^{-2}
$[Z]$	−0.81
M_*	~0.6 M_{\odot}
Progenitor	1–1.5 M_{\odot}
Age	>1000 yr
Distance	2.1 kpc
Nebula	
Abundances	He:11.11,C:8.49,N:7.89,O:8.30, ($\log X/H+12$) Ne:7.67,P:5.21,S:6.15,Cl:4.20, Ar:5.95,Fe:5.01,Others:[X/H]=−0.81
Geometry	Spherical
Shell size	$R_{\text{in}}=0.8''$ (0.008 pc)/ $R_{\text{out}}=2.6''$ (0.027 pc)
input density profile	See Fig.3(b)
ϵ	0.25
$\log F(\text{H}\beta)$	−10.22 $\text{erg s}^{-1} \text{cm}^{-2}$ (de-redden)
$m_g(\text{CLOUDY})$	0.023 M_{\odot}
Dust in Nebula	
Composition	PAHs,AC,SiC,MgS
Grain size	0.5 & 0.005 μm (See text in detail)
Grain shape	CDE for MgS, spherical for the others
$T_d(\text{CLOUDY})^a$	90–267 K (See text)
$T_d(\text{BB FITTING})^b$	160–200 K
$m_d(\text{CLOUDY})^a$	3.44(−4) M_{\odot}
$m_d(\text{BB FITTING})^b$	4.81(−6)–9.27(−6) M_{\odot}
$m_d(\text{TOT.})^c$	3.49(−4)–3.53(−4) M_{\odot}
$m_d/m_g(\text{CLOUDY})$	1.52(−2)

NOTE. — The accuracy of $\log(X/H) + 12$ is 0.3 dex. AC stands for amorphous carbon.

^a The temperature and total mass of PAHs, AC, and SiC grains derived by CLOUDY.

^b The temperature and mass of MgS grains derived by the modified blackbody fitting.

^c The total mass of PAHs, AC, SiC, and MgS grains.

tween the observed intensity ratios of C_{60} 7.0, 8.5, 17.3 to 18.9 μm and the theoretical predictions (see their Figs. 5 and 6). In Tc1, the intensity peak of C_{60} 8.5 μm is 6400–9700 AU from the central star, while that of dust components is nearby the central star. It would be interesting that the intensity of the 11.2 μm feature peaks ~ 3000 AU away from the central star on the other side of C_{60} 8.5 μm (see their Fig.3), because HACs seem to have a spectral peak around 11.2 μm (Jones 2012).

4.3.2. Destruction of PAH clusters

Cami et al. (2010) argued that fullerenes are not formed from HACs, because if fullerenes formed by HAC decomposition process, fullerenes should be observed more frequently in objects with PAHs. Cami et al. (2011) suggested that fullerenes are products of the destruction of large PAHs (>60 C atoms) by the stellar wind shock ($\sim 100 \text{ km s}^{-1}$). PAHs first lose their peripheral H-atoms in the shock and in the post shock gas, and then the resulting carbon clusters can assemble into fullerenes.

4.3.3. Photo-chemical process of PAH clusters

In the reflection nebula NGC 7023, Sellgren et al. (2010) show that the C_{60} 18.9 μm emission peaks on the central star, while the PAH 16.4 μm emission is brightest between the regions of strong 18.9 μm and the H_2 0-0S(1) 17 μm emission. Berné & Tielens (2012) found that the abundance of C_{60} and PAHs in this nebula increases and decreases, respectively,

TABLE 14
THE PREDICTED RELATIVE FLUXES BY THE CLOUDY MODELS.

Ions	λ_{lab}	Type	$I(\lambda)_{\text{obs}}$	$I(\lambda)_{\text{cloudy}}$	
He ⁺	4387.93 Å	RL	2.38(-1)	2.69(-1)	
	4471.47 Å	RL	1.72(0)	2.22(0)	
	4921.93 Å	RL	4.64(-1)	5.84(-1)	
	5876.66 Å	RL	6.16(0)	6.76(0)	
	6678.16 Å	RL	1.60(0)	1.74(0)	
	7281.35 Å	RL	3.19(-1)	4.70(-1)	
C ²⁺	1906/09 Å	CEL	<5.03(+1)	4.52(+1)	
N ⁺	5754.64 Å	CEL	5.87(0)	6.92(0)	
	6548.04 Å	CEL	5.89(+1)	6.77(+1)	
	6583.46 Å	CEL	1.90(+2)	2.00(+2)	
N ²⁺	1750 Å	CEL	1.41(0)	1.04(0)	
O ⁺	3726.03 Å	CEL	5.54(+1)	6.97(+1)	
	3728.81 Å	CEL	1.97(+1)	2.94(+1)	
	7320/30 Å	CEL	2.58(+1)	4.39(+1)	
	O ²⁺	4361.21 Å	CEL	1.37(-1)	1.80(-1)
O ²⁺	4958.91 Å	CEL	6.44(0)	6.07(0)	
	5006.84 Å	CEL	1.85(+1)	1.83(+1)	
	Ne ⁺	12.81 μm	CEL	3.09(+1)	3.18(+1)
	P ⁺	1.15 μm	CEL	1.22(-1)	1.31(-1)
S ⁺	1.19 μm	CEL	3.41(-1)	3.93(-1)	
	4068.60 Å	CEL	1.79(0)	1.27(0)	
	4076.35 Å	CEL	6.34(-1)	4.07(-1)	
S ²⁺	6716.44 Å	CEL	4.42(-1)	4.56(-1)	
	6730.81 Å	CEL	1.08(0)	9.08(-1)	
	6312.10 Å	CEL	3.23(-1)	5.50(-1)	
	9068.60 Å	CEL	3.22(0)	3.89(0)	
Cl ⁺	18.71 μm	CEL	1.40(0)	3.65(0)	
	8578.69 Å	CEL	1.19(-1)	5.94(-2)	
	9123.60 Å	CEL	7.76(-2)	1.57(-2)	
Cl ²⁺	5517.66 Å	CEL	2.88(-2)	3.24(-2)	
	5537.60 Å	CEL	7.22(-2)	7.62(-2)	
	Ar ²⁺	5191.82 Å	CEL	1.86(-2)	2.62(-2)
Fe ²⁺	7135.80 Å	CEL	2.46(0)	3.04(0)	
	8.99 μm	CEL	3.06(0)	1.91(0)	
	4701.53 Å	CEL	6.89(-2)	6.62(-2)	
	4754.69 Å	CEL	3.86(-2)	2.70(-2)	
	4769.43 Å	CEL	5.32(-2)	2.22(-2)	
	4881.00 Å	CEL	4.93(-2)	7.07(-2)	
	5270.40 Å	CEL	7.06(-2)	8.85(-2)	
Bands	λ_{center}	$\Delta\lambda$	$I(\lambda)_{\text{obs}}$	$I(\lambda)_{\text{cloudy}}$	
<i>B</i>	0.40 μm	0.300 μm	4.05(+2)	4.36(+2)	
<i>J</i>	1.24 μm	0.162 μm	1.14(+2)	1.24(+2)	
<i>H</i>	1.66 μm	0.251 μm	9.21(+1)	1.12(+2)	
<i>Ks</i>	2.16 μm	0.262 μm	8.36(+1)	8.01(+1)	
<i>WISE1</i>	3.353 μm	0.663 μm	1.15(+2)	1.32(+1)	
<i>WISE2</i>	4.603 μm	1.042 μm	1.43(+2)	1.27(+2)	
<i>AKARI1</i>	9.22 μm	4.104 μm	1.62(+3)	1.01(+3)	
<i>IRS1</i>	10.30 μm	1.000 μm	2.21(+2)	2.18(+2)	
<i>IRS2</i>	11.30 μm	1.000 μm	6.54(+2)	6.81(+2)	
<i>IRS3</i>	12.50 μm	1.000 μm	5.14(+2)	5.14(+2)	
<i>IRS4</i>	13.50 μm	0.600 μm	2.08(+2)	2.56(+2)	
<i>AKARI2</i>	66.70 μm	20.2 μm	4.49(+2)	5.04(+2)	
<i>AKARI3</i>	89.20 μm	39.9 μm	3.70(+2)	3.47(+2)	

when approaching the ionizing star HD200775 ($T_{\text{eff}} \sim 19000$ K, e.g. Alecian et al. 2008). They proposed that fullerenes are products of the photo-chemical processing of large PAHs. Such large PAH clusters could be from HACs as described above.

4.3.4. Comparison between C₆₀ PNe

Which explanations are more suitable to describe fullerene formation in Galactic PNe? To answer this question, we checked the properties of the central stars and the dust components, as summarized in Table 15. García-Hernández et al.

(2010) detected fullerenes in K3-54; however, the properties of the central star and gas-phase elemental abundances are unknown. Therefore, we do not list this PN. The progenitor masses M_{prop} and the evolutionary age after AGB phase in the fifth and sixth columns are estimated from the location on the H-burning tracks of Vassiliadis & Wood (1994) with $Z=0.02$ for Tc1 and $Z=0.004$ for the others. Prior to our study, the C and Ne abundances in M1-12 were not well known. However, using the measured $T_e(\text{S III})$ and $n_e(\text{S II})$, the intensities of the C II 6462 Å, and the de-reddened H β flux given by Henry et al. (2010), and our measured $F([\text{Ne II}] 12.8 \mu\text{m}) = 6.83(-12)$ erg s⁻¹ cm⁻², we estimated C and Ne abundances. To do so, we assumed that $\text{C}/\text{H} = (\text{Ar}/\text{Ar}^{2+}) \times \text{C}^{2+}/\text{H}^+$ and $\text{Ne}/\text{H} = \text{Ne}^+/\text{H}^+$. We derived C^{2+}/H^+ and Ne^+/H^+ as 2.06(-3) and 5.96(-5), respectively. In the gas-phase abundances of all objects listed in Table 15, the N, O, Ne, S, Cl, Ar, and Kr abundances are derived from CELs, and the He and C abundances from RLs. The CEL C abundances in M1-12 and M1-20 are unknown due to a lack of UV spectra.

We found the following common properties in these PNe: (1) relatively cool central stars except for M1-20, (2) young age, (3) broad 6-9, 10-14, and 30 μm features, (4) a strong stellar wind. In the UV spectra taken by *IUE* and *FUSE*, we found that Tc1 shows the P-Cygni profile of Ly α 1215 Å. There are no data with enough signal-to-noise ratio to check for the presence of P-Cygni Ly α profiles in the other PNe. However, since these PNe have the Wolf-Rayet-like central stars ([WC10,11] and weak emission line central star, wel), which show broad C III,IV lines ($\gtrsim 60$ km s⁻¹ at FWHM), there would be a strong wind for each.

From properties (1) and (2), the short time duration of weak radiation from the central star would be an essential condition for fullerenes to survive or to be observed for a long time. The observational fact that all fullerene PNe have cool central stars and low-excitation nebulae, except for M1-20, matches the detection of the C₆₀ in a proto PN and two post AGB stars by Zhang & Kwok (2011) and Gielen et al. (2011), respectively; these sources have cool central stars (21500 K in IRAS01005+7910; 6250 and 6000 K in IRAS06338+5333 and HD52961, respectively). Property (3) implies that fullerenes might not be formed from HACs in Galactic PNe. HACs reproduce 6-9, 10-14, ~20, and ~30 μm broad features. If the 30 μm feature is from HACs, we should see the ~20 μm feature, too. However, not all Galactic fullerene PNe show the ~20 μm feature. As we mentioned in Section 2.6.2, however, the strength of 20 and 30 μm features largely depends on H-content, grain size, etc. At present, therefore, we cannot rule out that fullerenes arise from the destruction of HACs. From property (4), the strong stellar wind would promote fullerene synthesis for young PNe and post-AGB stars with cool central stars. In M1-11, as we mentioned in Section 2.3, the H₂ lines within the optical diameter are excited by both UV fluorescence and shocks. Lumsden et al. (2001) observed the *HK*-band spectra of M1-12 and M1-20. However H₂ 1-0S(1) and 2-1S(1) lines are not detected.

If C₆₀ is from large PAH clusters, the spatial distribution of PAHs and C₆₀ would be similar to that in NGC7023. If C₆₀ is from HACs, the spatial distribution of C₆₀ would be similar to that in Tc1, as shown in Fig.3 of Bernard-Salas et al. (2012). At present, destruction of HACs seems to be the most plausible scenario for fullerene formation in Galactic PNe, including M1-11. If so, the spatial distribution of C₆₀ in M1-11 would be similar to that in Tc1. To advance our understanding

TABLE 15
PHYSICAL PARAMETERS OF C₆₀ DETECTED GALACTIC PNE.

Nebula	T_{eff} (K)	L_* (L_{\odot})	$\log g$ (cm s^{-2})	$M_{\text{prop.}}^a$ (M_{\odot})	Age ^a (yrs)	Type of Central star	Gas-phase abundances ^b (He/C/N/O/Ne/ (P/S/Cl/Ar/Kr))	Dust	T_{C60} (K)	Ref.
M1-11	31 950	4510	3.5	1-1.5	>1000	[WC10-11]	10.75/9.34/8.08/8.62/7.68/ 4.88/6.15/4.45/5.66/3.81	PAHs,SiC?,AC,MgS?	399	(1),(2),(3)
M1-12	33 000	8700	3.4	~1.5	~1000	[WC10-11]	10.54/9.40/7.55/8.11/7.78/ ... /6.25/5.01/5.40/3.83	PAHs,SiC?,AC,MgS?	345	(1),(2),(3),(4),(5)
Tc1	34 700	6900	3.4	~2	<1000	Of(H)	>10.78/8.56/7.56/8.42/7.80/ 5.30/6.45/4.97/6.71/ ...	(weak)PAHs?,AC,MgS?	339	(1),(4),(6),(7),(8),(9)
M1-20	53 000	8300	5.0	1-1.5	<3900	wel	10.98/8.74/7.94/8.58/8.21/ ... /6.68/4.93/5.85/ ...	PAHs?,SiC?,AC,MgS?	425	(1),(4),(7),(10),(11),(12)

REFERENCES. — (1) This work; (2) Weidmann & Gamen (2011a); (3) Sterling & Dinerstein 2008; (4) Zhang & Kwok (1993); (5) Henry et al. (2010); (6) Cami et al. (2010); (7) García-Hernández et al. (2010); (8) Pottasch et al. (2011); (9) Weidmann & (2011b); (10) Wang & Liu (2007); (11) Górný et al. (2009); (12) Kaler & Jacoby (1991)

^a The values are estimated from the location on the H-burning tracks with $Z=0.02$ for Tc1 and $Z=0.004$ for the others by Vassiliadis & Wood (1994).

^b The number density relative to the hydrogen is defined as $\log H=12$. The C abundance is derived from RLs except for Tc1. The C in Tc1 is derived from CEL. The N, O, and Ne abundances are derived from CELs. The predicted abundances in M1-11 by CLOUDY are listed in Table 13.

of what kinds of conditions in which fullerenes can be formed and survive, the high-resolution spatial observations are necessary to investigate the spatial variation of HACs, PAHs, C₆₀, and dust components.

5. SUMMARY AND FUTURE WORK

We performed multiwavelength observations for the young PN M1-11 to investigate elemental abundances and dust mass, and we discussed its evolutionary status from its progenitor. We found a large discrepancy between the RL and the CEL O & N abundances. The RL C/O abundance ratio is <1 . If the RL C/O ratio represents the chemistry of the PN, the nebula is O-rich. The RL O abundance is much larger than that predicted by AGB nucleosynthesis models, while the CEL O abundance is close to that predicted by the models. The CEL C and O would be reliable in M1-11. Therefore, we estimated the CEL C abundance using the relation between $\text{ADF}(\text{C}^{2+})$ and $\text{ADF}(\text{O}^{2+})$ among 56 Galactic PNe, and we obtained a CEL C/O, implying the possibility that M1-11 could be C-rich. We estimated the CEL C and O abundances through the SED model.

In the *AKARI*/IRC, VLT/VISIR, and *Spitzer*/IRS spectra, 3.3, 8.6, and 11.3 μm PAH bands and broad 10-13 and 30 μm features are visible. SiC and MgS could be the main contributors to the broad 10-13 and 30 μm features, respectively. We detect broad emission from ~ 16 -22 μm ; however, it is still unclear whether this feature is from C-rich or O-rich dust. We also detect three C₆₀ lines in the VISIR and *Spitzer* data of M1-11. The presence of C₆₀ might be explained by destruction of HACs in this PN. As shown in Table 15, fullerene-containing Galactic PNe seem to have central star properties, gas-phase abundances, and dust composition in common. Except for M1-20, most of these PNe that have fullerenes seem to have cool central stars. The radiation field around a relatively low temperature star is intrinsically weak. Moreover, the surrounding shell structure around such a low temperature star might have diluted the stellar UV flux. Such circumstances must have played a favorable role for fullerenes

to survive in the circumstellar medium.

Through ~ 0.1 -90 μm SED modeling, we estimate the dust mass and the properties of the central star and the nebula. Our current analysis indicates that the progenitor would be a 1-1.5 M_{\odot} star. The observed abundances and the predicted CEL C and C/O can be explained by an AGB nucleosynthesis model for 1.5 M_{\odot} progenitors with $Z=0.004$. M1-11 is possibly a C-rich PN.

For a future study on M1-11, high spatial resolution spectroscopy or narrow-band imaging would be necessary to resolve the spatial distribution of PAHs, C₆₀, HAC, and dust components to check how these co-exist in the nebulae. It is essential to investigate the properties of the central stars, the excitation degree of the nebulae, and the dust composition in young and low-excitation PNe such as M1-11 to understand the condition in which fullerenes form and survive.

ACKNOWLEDGMENTS

We are grateful to the anonymous referee for a careful review and many valuable suggestions. The authors thank Prof. Karen Kwitter for providing their M1-11 spectrum. M.O. acknowledges funding support from STScI GO-1129.01-A, NASA NAO-50-12595, and STScI DDRF D0101.90128. FK acknowledges support from the National Science Council in the form of grant NSC100-2112-M-001-023-MY3. S.H. acknowledges support by the Basic Research Program through the National Research Foundation of Korea by the Ministry of Education, Science and Technology (NRF-2011-0005077). This work is mainly based on data collected at the Subaru Telescope, which is operated by the National Astronomical Observatory of Japan (NAOJ). This work is in part based on *HST* and *IUE* archive data downloaded from the *MAST* and *AKARI* archive data from *DARTS*. This work is in part based on archival data obtained with the *Spitzer* Space Telescope, which is operated by the Jet Propulsion Laboratory, California Institute of Technology under a contract with NASA. Support for this work was provided by an award issued by JPL/Caltech.

APPENDIX

OBSERVED LINE LISTS

The detected lines in the Subaru/HDS and OAO/ISLE are listed in Tables 16 and 17, respectively.

TABLE 16
 THE DETECTED LINES IN THE HDS OBSERVATIONS.

λ_{lab} (Å)	Ion	$f(\lambda)$	$I(\lambda)$ [$I(\text{H}\beta)=100$]	λ_{lab} (Å)	Ion	$f(\lambda)$	$I(\lambda)$ [$I(\text{H}\beta)=100$]	λ_{lab} (Å)	Ion	$f(\lambda)$	$I(\lambda)$ [$I(\text{H}\beta)=100$]
3661.21	H31	0.335	0.681 ± 0.111	4574.88	[Mn III]	0.083	0.059 ± 0.010	5537.60	[Cl III]	-0.149	0.072 ± 0.012
3662.26	H30	0.335	0.698 ± 0.073	4591.12	S II	0.078	0.082 ± 0.015	5554.83	O I	-0.152	0.100 ± 0.023
3663.40	H29	0.335	0.483 ± 0.062	4630.54	N II	0.066	0.055 ± 0.007	5577.20	[O I]	-0.156	0.040 ± 0.008
3664.68	H28	0.335	0.865 ± 0.075	4634.12	N III	0.065	0.447 ± 0.027	5659.60	C III	-0.169	0.054 ± 0.011
3666.10	H27	0.334	0.465 ± 0.063	4635.32	Fe II	0.065	0.033 ± 0.004	5666.63	N II	-0.171	0.101 ± 0.048
3667.71	H26	0.334	0.583 ± 0.079	4640.03	C III	0.063	0.012 ± 0.001	5690.43	Si I	-0.174	0.038 ± 0.017
3669.46	H25	0.334	1.135 ± 0.082	4640.64	N III	0.063	0.115 ± 0.004	5695.92	C III	-0.175	2.113 ± 0.036
3671.38	H24	0.333	0.961 ± 0.063	4641.81	O II	0.063	0.026 ± 0.001	5730.66	N II	-0.181	0.043 ± 0.013
3673.74	H23	0.333	1.182 ± 0.075	4641.85	N III	0.063	0.044 ± 0.002	5754.60	[N II]	-0.185	5.986 ± 0.077
3674.84	He II	0.333	0.174 ± 0.045	4649.14	O II	0.060	0.022 ± 0.006	5826.42	C III	-0.196	0.122 ± 0.024
3676.36	H22	0.332	1.025 ± 0.076	4650.84	O II	0.060	0.031 ± 0.007	5831.70	N III?	-0.196	0.041 ± 0.012
3679.35	H21	0.332	1.384 ± 0.074	4652.05	C III	0.060	0.213 ± 0.019	5875.66	He I	-0.203	6.155 ± 0.083
3682.81	H20	0.331	1.482 ± 0.058	4658.64	C IV	0.058	0.137 ± 0.008	5958.39	O I	-0.215	0.129 ± 0.021
3686.83	H19	0.330	1.569 ± 0.054	4676.23	O II	0.053	0.096 ± 0.023	6046.23	O I	-0.228	0.239 ± 0.028
3691.55	H18	0.329	2.015 ± 0.097	4685.68	He II	0.050	0.078 ± 0.021	6074.20	C I	-0.232	0.057 ± 0.014
3697.15	H17	0.328	1.853 ± 0.065	4701.53	[Fe III]	0.045	0.069 ± 0.008	6077.90	C II	-0.232	0.075 ± 0.021
3703.65	H16	0.327	1.741 ± 0.051	4713.17	He I	0.042	0.260 ± 0.012	6267.81	[V II]?	-0.258	0.041 ± 0.010
3711.97	H15	0.325	2.328 ± 0.052	4754.69	[Fe III]	0.030	0.039 ± 0.009	6300.34	[O I]	-0.263	2.203 ± 0.041
3715.08	O III	0.324	0.296 ± 0.041	4769.43	[Fe III]	0.025	0.053 ± 0.006	6312.10	[S III]	-0.264	0.323 ± 0.015
3721.94	H14	0.323	2.583 ± 0.074	4789.57	N II	0.017	0.051 ± 0.016	6347.09	Si II	-0.269	0.126 ± 0.017
3726.03	[O II]	0.322	55.380 ± 0.526	4861.33	H4	0.000	100.000 ± 0.130	6363.78	[O I]	-0.271	0.748 ± 0.021
3728.81	[O II]	0.322	19.692 ± 0.302	4881.00	[Fe III]	-0.005	0.049 ± 0.005	6527.24	[N II]	-0.293	0.030 ± 0.004
3734.37	H13	0.321	2.590 ± 0.064	4921.93	He I	-0.016	0.464 ± 0.007	6548.10	[N II]	-0.296	58.851 ± 0.989
3750.15	H12	0.317	3.438 ± 0.051	4924.54	[Fe III]	-0.017	0.016 ± 0.008	6562.77	H3	-0.298	285.000 ± 4.160
3770.63	H11	0.313	3.833 ± 0.069	4931.80	[O III]	-0.019	0.136 ± 0.026	6578.01	C II	-0.300	0.499 ± 0.012
3797.90	H10	0.307	7.047 ± 0.065	4934.08	Ba II	-0.019	0.016 ± 0.004	6583.50	[N II]	-0.300	190.199 ± 4.767
3819.60	He I	0.302	0.363 ± 0.034	4958.91	[O III]	-0.026	6.440 ± 0.031	6678.16	He I	-0.313	1.600 ± 0.028
3835.38	H9	0.299	8.950 ± 0.083	5006.84	[O III]	-0.038	18.544 ± 0.082	6688.79	C I	-0.314	0.050 ± 0.012
3889.05	H8	0.286	13.681 ± 0.100	5015.68	He I	-0.040	0.989 ± 0.004	6701.49	N II	-0.316	0.067 ± 0.008
3918.97	C II	0.279	0.242 ± 0.032	5017.22	N II	-0.040	0.014 ± 0.004	6716.44	[S II]	-0.318	0.442 ± 0.016
3920.68	C II	0.279	0.510 ± 0.025	5030.33	[Fe IV]	-0.043	0.036 ± 0.014	6730.82	[S II]	-0.320	1.084 ± 0.027
3964.73	He I	0.267	0.598 ± 0.023	5032.07	C II	-0.044	0.106 ± 0.018	6744.33	C III	-0.322	0.125 ± 0.017
3970.07	H7	0.266	18.792 ± 0.104	5041.02	Si II	-0.046	0.043 ± 0.008	7002.17	O I	-0.356	0.210 ± 0.009
4026.18	He I	0.251	0.949 ± 0.020	5047.74	He I	-0.048	0.105 ± 0.006	7018.63	Ca I]?	-0.358	0.023 ± 0.006
4056.91	N II	0.243	0.254 ± 0.029	5055.98	Si II	-0.050	0.119 ± 0.011	7037.25	C III	-0.361	0.139 ± 0.013
4068.60	[S II]	0.239	1.790 ± 0.047	5080.49	[Ni III]	-0.056	0.137 ± 0.023	7065.18	He I	-0.364	2.276 ± 0.036
4076.35	[S II]	0.237	0.634 ± 0.055	5121.83	C II	-0.065	0.063 ± 0.009	7065.71	He I	-0.364	0.334 ± 0.011
4089.30	O III	0.233	0.095 ± 0.014	5131.25	[Krv]	-0.067	0.140 ± 0.015	7101.07	Ca I	-0.369	0.020 ± 0.006
4101.73	H6	0.230	27.822 ± 0.127	5143.29	[Fe III]	-0.070	0.048 ± 0.003	7135.80	[Ar III]	-0.374	2.457 ± 0.042
4128.66	N II	0.222	0.216 ± 0.052	5145.17	C II	-0.070	0.092 ± 0.005	7179.88	Ca I	-0.380	0.066 ± 0.006
4143.76	He I	0.217	0.175 ± 0.019	5145.75	[Fe VI]?	-0.071	0.018 ± 0.008	7231.33	C II	-0.387	0.216 ± 0.012
4267.15	C II	0.180	0.614 ± 0.027	5146.45	[Fe III]	-0.071	0.115 ± 0.007	7231.48	Ca I	-0.387	0.077 ± 0.007
4307.44	N III?	0.167	0.099 ± 0.019	5191.82	[Ar III]	-0.081	0.019 ± 0.004	7236.20	Ca I	-0.387	0.058 ± 0.004
4317.19	C III	0.164	0.120 ± 0.018	5197.90	[N I]	-0.082	0.201 ± 0.009	7236.42	C II	-0.387	0.436 ± 0.011
4340.46	H5	0.157	46.900 ± 0.174	5200.26	[N I]	-0.083	0.123 ± 0.008	7236.80	C I]	-0.387	0.057 ± 0.004
4352.52	N II	0.153	0.028 ± 0.011	5270.40	[Fe III]	-0.098	0.071 ± 0.004	7237.17	C II	-0.387	0.071 ± 0.005
4363.21	[O III]	0.149	0.137 ± 0.015	5274.78	[Mn II]	-0.099	0.055 ± 0.009	7254.53	O I	-0.390	0.263 ± 0.012
4368.24	O I	0.148	0.317 ± 0.029	5298.88	[Fe II]	-0.104	0.118 ± 0.009	7281.35	He I	-0.393	0.319 ± 0.013
4369.56	O III	0.147	0.137 ± 0.031	5304.54	C III	-0.105	0.063 ± 0.016	7318.92	[O II]	-0.398	3.837 ± 0.077
4377.77	Mn II	0.145	0.060 ± 0.016	5342.43	C II	-0.112	0.032 ± 0.004	7319.99	[O II]	-0.398	11.165 ± 0.193
4387.93	He I	0.142	0.238 ± 0.008	5347.89	O II	-0.113	0.018 ± 0.005	7329.67	[O II]	-0.400	5.513 ± 0.103
4414.90	O II	0.133	0.191 ± 0.017	5351.81	[Cr III]	-0.114	0.047 ± 0.006	7330.73	[O II]	-0.400	5.284 ± 0.102
4416.98	O II	0.132	0.223 ± 0.020	5365.10	[Mn III]	-0.117	0.022 ± 0.004	7442.20	C IV	-0.415	0.076 ± 0.007
4471.47	He I	0.115	1.718 ± 0.030	5461.91	Fe II	-0.135	0.038 ± 0.021	7452.60	[Fe II]	-0.416	0.119 ± 0.010
4541.59	He II	0.094	0.249 ± 0.021	5494.69	[Fe III]	-0.141	0.064 ± 0.014	7457.90	C II]	-0.417	0.044 ± 0.005
4571.10	Mg I]	0.084	0.221 ± 0.017	5517.66	[Cl III]	-0.145	0.029 ± 0.006	7468.31	N I	-0.418	0.103 ± 0.007

TABLE 17
THE DETECTED LINES IN THE ISLE OBSERVATIONS.

λ_{vac} (μm)	Ion	$f(\lambda)$	$F(\lambda)$ ($\text{erg s}^{-1} \text{cm}^{-2}$)	$I(\lambda)$ ($I(\text{Pa}\beta, \text{Br}\gamma)=100$)
1.129	O I	-0.715	$7.34(-14) \pm 4.51(-15)$	2.535 ± 0.188
1.147	[P II]	-0.722	$2.23(-14) \pm 3.20(-15)$	0.755 ± 0.113
1.162	H ₂ 2-0 S(1)	-0.728	$8.51(-15) \pm 9.80(-16)$	0.283 ± 0.035
1.175	O I?	-0.733	$1.76(-14) \pm 1.29(-15)$	0.577 ± 0.049
1.186	H ₂ 3-1 S(3)	-0.736	$1.62(-14) \pm 9.60(-16)$	0.525 ± 0.038
1.189	[P II]	-0.737	$6.50(-14) \pm 1.06(-15)$	2.106 ± 0.095
1.190	H ₂ 2-0 S(0)	-0.738	$6.46(-15) \pm 1.06(-15)$	0.209 ± 0.035
1.194	Ca I?	-0.739	$5.12(-15) \pm 1.37(-15)$	0.165 ± 0.045
1.197	He I	-0.740	$8.09(-15) \pm 8.40(-16)$	0.260 ± 0.029
1.199	N III?	-0.741	$7.32(-15) \pm 6.80(-16)$	0.235 ± 0.024
1.208	H ₂ 3-1 S(2)	-0.744	$8.43(-15) \pm 7.90(-16)$	0.268 ± 0.028
1.219	Cl?	-0.748	$4.69(-15) \pm 7.90(-16)$	0.147 ± 0.026
1.221	Ca I?	-0.748	$3.44(-15) \pm 7.90(-16)$	0.108 ± 0.025
1.226	H ₂ 4-2 S(5)	-0.750	$4.79(-15) \pm 6.80(-16)$	0.150 ± 0.022
1.229	C II	-0.751	$1.05(-14) \pm 6.60(-16)$	0.327 ± 0.025
1.230	Si I?	-0.751	$7.11(-15) \pm 6.60(-16)$	0.221 ± 0.023
1.233	H ₂ 3-1S(1)	-0.752	$2.07(-14) \pm 8.80(-16)$	0.642 ± 0.039
1.239	H ₂ 2-0 Q(1)	-0.754	$1.50(-14) \pm 1.08(-15)$	0.462 ± 0.039
1.242	H ₂ 4-2 S(4) + H ₂ 2-0Q(2)	-0.755	$7.44(-15) \pm 1.05(-15)$	0.229 ± 0.034
1.247	Si I?	-0.757	$4.84(-15) \pm 2.08(-15)$	0.149 ± 0.064
1.247	H ₂ 2-0 Q(3)	-0.757	$8.61(-15) \pm 8.50(-16)$	0.264 ± 0.028
1.253	He I	-0.759	$2.05(-14) \pm 9.90(-16)$	0.625 ± 0.040
1.255	H ₂ 2-0 Q(4)	-0.759	$2.25(-15) \pm 8.70(-16)$	0.069 ± 0.027
1.257	[Fe II]	-0.760	$6.52(-15) \pm 7.50(-16)$	0.198 ± 0.024
1.262	H ₂ 4-2 S(3)	-0.761	$1.25(-14) \pm 8.90(-16)$	0.379 ± 0.031
1.262	H ₂ 3-1S(0)	-0.761	$9.17(-15) \pm 8.90(-16)$	0.278 ± 0.029
1.264	H ₂ 2-0Q(5)	-0.762	$3.23(-15) \pm 1.15(-15)$	0.098 ± 0.035
1.265	[Fe IV]?	-0.762	$4.18(-15) \pm 9.10(-16)$	0.126 ± 0.028
1.2788	He I	-0.766	$4.16(-14) \pm 1.31(-15)$	1.242 ± 0.066
1.2794	He I	-0.767	$1.92(-14) \pm 1.31(-15)$	0.573 ± 0.046
1.282	Pa β	-0.767	$3.36(-12) \pm 3.05(-15)$	100.000 ± 4.290
1.285	H ₂ 4-2 S(2)	-0.768	$8.42(-15) \pm 8.30(-16)$	0.250 ± 0.027
2.034	H ₂ 1-0 S(2)	-0.889	$1.97(-14) \pm 1.48(-15)$	3.476 ± 0.315
2.042	H ₂ 8-6 O(3)	-0.890	$1.43(-14) \pm 1.63(-15)$	2.519 ± 0.314
2.059	He I	-0.891	$2.74(-13) \pm 3.83(-15)$	48.053 ± 2.534
2.074	H ₂ 2-1 S(3)	-0.893	$2.15(-14) \pm 1.33(-15)$	3.758 ± 0.301
2.102	Si I?	-0.895	$9.27(-15) \pm 9.50(-16)$	1.610 ± 0.184
2.113	He I	-0.896	$7.77(-15) \pm 1.27(-15)$	1.346 ± 0.230
2.122	H ₂ 1-0 S(1)	-0.897	$4.90(-14) \pm 1.05(-15)$	8.471 ± 0.468
2.138	Mg II	-0.898	$4.67(-15) \pm 5.30(-16)$	0.805 ± 0.100
2.144	Mg II	-0.898	$4.88(-15) \pm 8.40(-16)$	0.840 ± 0.151
2.154	H ₂ 2-1 S(2)	-0.899	$8.00(-15) \pm 8.10(-16)$	1.373 ± 0.156
2.162	He I	-0.900	$9.78(-15) \pm 3.30(-16)$	1.676 ± 0.103
2.166	H I (Br γ)	-0.900	$5.84(-13) \pm 5.23(-15)$	100.000 ± 5.186
2.171	O I	-0.900	$8.54(-15) \pm 1.08(-15)$	1.461 ± 0.199
2.189	He II	-0.902	$6.50(-15) \pm 7.60(-16)$	1.108 ± 0.141
2.199	[Kr III]	-0.902	$1.89(-14) \pm 1.22(-15)$	3.215 ± 0.265
2.201	H ₂ 3-2 S(3)	-0.903	$6.70(-15) \pm 1.22(-15)$	1.139 ± 0.215
2.205	C II?	-0.903	$2.82(-15) \pm 7.40(-16)$	0.479 ± 0.128
2.224	H ₂ 1-0 S(0)	-0.904	$1.07(-14) \pm 1.11(-15)$	1.811 ± 0.210
2.248	H ₂ 2-1 S(1)	-0.906	$1.99(-14) \pm 1.20(-15)$	3.353 ± 0.265
2.287	H ₂ 3-2 S(2)	-0.908	$4.00(-15) \pm 1.80(-15)$	0.669 ± 0.303

REFERENCES

- Alecian, E., Catala, C., Wade, G. A., et al. 2008, *MNRAS*, 385, 391
- Allen, D. A., Baines, D. W. T., Blades, J. C., & Whittet, D. C. B. 1982, *MNRAS*, 199, 1017
- Baker, J. G., & Menzel, D. H. 1938, *ApJ*, 88, 52
- Begemann, B., Dorschner, J., Henning, T., Mutschke, H., & Thamm, E. 1994, *ApJ*, 423, L71
- Benjamin, R. A., Skillman, E. D., & Smits, D. P. 1999, *ApJ*, 514, 307
- Bernard-Salas, J., Cami, J., Peeters, E., et al. 2012, *ApJ*, 757, 41
- Bernard-Salas, J. et al. 2009, *ApJ*, 699, 1541
- Berné, O., & Tielens, A. G. G. M. 2012, *Proceedings of the National Academy of Science*, 109, 401
- Bohren, C. F., & Huffman, D. R., "Absorption and Scattering of Light by Small Particles", 1983, New York: Wiley, 1983,
- Bregman, J. D., Allamandola, L. J., Witteborn, F. C., Tielens, A. G. G. M., & Geballe, T. R. 1989, *ApJ*, 344, 791
- Cahn, J. H., Kaler, J. B., & Stanghellini, L. 1992, *A&AS*, 94, 399
- Cami, J., Bernard-Salas, J., Peeters, E., & Malek, S. E. 2010, *Science*, 329, 1180
- Cami, J., Bernard-Salas, J., Peeters, E., & Malek, S. E. 2011, *IAU Symposium*, 280, 216
- Cardelli, J. A., Clayton, G. C., & Mathis, J. S. 1989, *ApJ*, 345, 245
- Cohen, M., Allamandola, L., Tielens, A. G. G. M., Bregman, J., Simpson, J. P., Witteborn, F. C., Wooden, D., & Rank, D. 1986, *ApJ*, 302, 737
- Desert, F.-X., Boulanger, F., & Puget, J. L. 1990, *A&A*, 237, 215
- Dopita, M. A., Vassiliadis, E., Wood, P. R., et al. 1997, *ApJ*, 474, 188
- Draine, B. T., "Physics of the Interstellar and Intergalactic Medium", 2011, Princeton University Press
- Fabian, D., Henning, T., Jäger, C., Mutschke, H., Dorschner, J., & Wehrhan, O. 2001, *A&A*, 378, 228
- Ferland, G. J., Korista, K. T., Verner, D. A., et al. 1998, *PASP*, 110, 761
- Fluks, M. A., Plez, B., The, P. S., de Winter, D., Westerlund, B. E., & Steenman, H. C. 1994, *A&AS*, 105, 311
- García-Hernández, D. A., Villaver, E., García-Lario, P., et al. 2012, *ApJ*, 760, 107
- García-Hernández, D. A. 2012, *IAU Symposium*, 283, 148
- García-Hernández, D. A., Iglesias-Groth, S., Acosta-Pulido, J. A., et al. 2011a, *ApJ*, 737, L30
- García-Hernández, D. A., Kameswara Rao, N., & Lambert, D. L. 2011b, *ApJ*, 729, 126
- García-Hernández, D. A., Manchado, A., García-Lario, P., et al. 2010, *ApJ*, 724, L39
- Gielen, C., Cami, J., Bouwman, J., Peeters, E., & Min, M. 2011, *A&A*, 536, A54
- Grishko, V. I., Tereszchuk, K., Duley, W. W., & Bernath, P. 2001, *ApJ*, 558, L129
- Górny, S. K., Chiappini, C., Stasińska, G., & Cuisinier, F. 2009, *A&A*, 500, 1089
- Henry, R. B. C., Kwitter, K. B., Jaskot, A. E., Balick, B., Morrison, M. A., & Milingo, J. B. 2010, *ApJ*, 724, 748
- Hony, S., Waters, L. B. F. M., & Tielens, A. G. G. M. 2001, *A&A*, 378, L41
- Hony, S., Tielens, A. G. G. M., Waters, L. B. F. M., & de Koter, A. 2003, *A&A*, 402, 211
- Hora, J. L., & Latter, W. B. 1994, *ApJ*, 437, 281
- Hora, J. L., & Latter, W. B. 1996, *ApJ*, 461, 288
- Houck, J. R., et al. 2004, *Proc. SPIE*, 5487, 62
- Idiart, T. P., Maciel, W. J., & Costa, R. D. D. 2007, *A&A*, 472, 101
- Jones, A. P. 2012, *A&A*, 542, A98
- Kaler, J. B., & Jacoby, G. H. 1991, *ApJ*, 372, 215
- Karakas, A. I. 2010, *MNRAS*, 403, 1413
- Kelly, D. M., & Hrivnak, B. J. 2005, *ApJ*, 629, 1040
- Kingsburgh, R. L., & Barlow, M. J. 1994, *MNRAS*, 271, 257
- Kwok, S., "Physics and Chemistry of the Interstellar Medium", 2007, University Science Books
- Lambert, D. L., Rao, N. K., Pandey, G., & Ivans, I. I. 2001, *ApJ*, 555, 925
- Leisy, P., & Dennefeld, M. 2006, *A&A*, 456, 451
- Liu, X.-W., Storey, P. J., Barlow, M. J., Danziger, I. J., Cohen, M., & Bryce, M. 2000, *MNRAS*, 312, 585
- Liu, X.-W., Luo, S.-G., Barlow, M. J., Danziger, I. J., & Storey, P. J. 2001, *MNRAS*, 327, 141
- Liu, Y., Liu, X.-W., Barlow, M. J., & Luo, S.-G. 2004, *MNRAS*, 353, 1251
- Lodders, K. 2003, *ApJ*, 591, 1220
- Lumsden, S. L., Puxley, P. J., & Hoare, M. G. 2001, *MNRAS*, 328, 419
- McCarthy, J. K., Mendez, R. H., & Kudritzki, R.-P. 1997, *Planetary Nebulae*, 180, 120
- Mendoza, C., & Zeppen, C. J. 1982, *MNRAS*, 199, 1025
- Min, M., Hovenier, J. W., & de Koter, A. 2003, *A&A*, 404, 35
- Murakami, H., et al. 2007, *PASJ*, 59, 369
- Noguchi, K., et al. 2002, *PASJ*, 54, 855
- Onaka, T., et al. 2007, *PASJ*, 59, 401
- Otsuka, M., Tajitsu, A., Hyung, S., & Izumiura, H. 2010, *ApJ*, 723, 658
- Otsuka, M., Meixner, M., Riebel, D., Hyung, S., Tajitsu, A., & Izumiura, H. 2011, *ApJ*, 729, 39
- Pegourie, B. 1988, *A&A*, 194, 335
- Phillips, J. P., & Ramos-Larios, G. 2005, *MNRAS*, 364, 849
- Phillips, J. P. 2003, *MNRAS*, 344, 501
- Pottasch, S. R., Surendiranath, R., & Bernard-Salas, J. 2011, *A&A*, 531, A23
- Ramos-Larios, G., & Phillips, J. P. 2005, *MNRAS*, 357, 732
- Rouleau, F., & Martin, P. G. 1991, *ApJ*, 377, 526
- Schutte, W. A., Tielens, A. G. G. M., & Allamandola, L. J. 1993, *ApJ*, 415, 397
- Scott, A., Duley, W. W., & Pinho, G. P. 1997, *ApJ*, 489, L193
- Seaton, M. J. 1979, *MNRAS*, 187, 73P
- Sellgren, K., Werner, M. W., Ingalls, J. G., et al. 2010, *ApJ*, 722, L54
- Shupe, D. L., Larkin, J. E., Knop, R. A., et al. 1998, *ApJ*, 498, 267
- Stanghellini, L., García-Hernández, D. A., García-Lario, P., et al. 2012, *ApJ*, 753, 172
- Stanghellini, L., García-Lario, P., García-Hernández, D. A., et al. 2007, *ApJ*, 671, 1669
- Stanghellini, L., Shaw, R. A., & Gilmore, D. 2005, *ApJ*, 622, 294
- Sterling, N. C., & Dinerstein, H. L. 2008, *ApJS*, 174, 158
- Storey, P. J., & Hummer, D. G. 1995, *MNRAS*, 272, 41
- Straniero, O., Chieffi, A., Limongi, M., et al. 1997, *ApJ*, 478, 332
- Tajitsu, A., & Tamura, S. 1998, *AJ*, 115, 1989
- Tayal, S. S. 2004a, *ApJS*, 150, 465
- Tayal, S. S. 2004b, *A&A*, 426, 717
- Tsamis, Y. G., Barlow, M. J., Liu, X.-W., Storey, P. J., & Danziger, I. J. 2004, *MNRAS*, 353, 953
- Van Kerckhoven, C., Hony, S., Peeters, E., et al. 2000, *A&A*, 357, 1013
- Vassiliadis, E., & Wood, P. R. 1994, *ApJS*, 92, 125
- Volk, K., Hrivnak, B. J., Matsuura, M., et al. 2011, *ApJ*, 735, 127
- Wang, W., & Liu, X.-W. 2007, *MNRAS*, 381, 669
- Weidmann, W. A., & Gamen, R. 2011a, *A&A*, 531, A172
- Weidmann, W. A., & Gamen, R. 2011b, *A&A*, 526, A6
- Wesson, R., Liu, X.-W., & Barlow, M. J. 2005, *MNRAS*, 362, 424
- Yanagisawa, K., Shimizu, Y., Okita, K., et al. 2006, *Proc. SPIE*, 6269, 7014
- Yanagisawa, K., et al. 2008, *Proc. SPIE*, 7014, 7014
- Zhang, C. Y., & Kwok, S. 1990, *A&A*, 237, 479
- Zhang, C. Y., & Kwok, S. 1993, *ApJS*, 88, 137
- Zhang, Y., & Kwok, S. 2011, *ApJ*, 730, 126
- Zhang, Y., & Liu, X.-W. 2003, *A&A*, 404, 545
- Zhang, K., Jiang, B. W., & Li, A. 2009, *ApJ*, 702, 680